AGU PUBLICATIONS

JGR

Journal of Geophysical Research: Atmospheres

RESEARCH ARTICLE
10.1002/2014JD022150

Key Points:
- AMTMs provide new abilities for gravity wave momentum flux estimates
- MTM and other instruments enable full definition of gravity wave parameters
- Momentum flux estimates for two packets reveal large magnitudes

Correspondence to:
D. C. Fritts,
dave@gats-inc.com

Citation:
Fritts, D. C., P.-D. Pautet, K. Bossert, M. J. Taylor, B. P. Williams, H. Iimura, T. Yuan, N. J. Mitchell, and G. Stober (2014), Quantifying gravity wave momentum fluxes with Mesosphere Temperature Mappers and correlative instrumentation, *J. Geophys. Res. Atmos.*, *119*, 13,583–13,603, doi:10.1002/2014JD022150.

Received 8 JUN 2014
Accepted 9 OCT 2014
Accepted article online 13 OCT 2014
Published online 16 DEC 2014

Quantifying gravity wave momentum fluxes with Mesosphere Temperature Mappers and correlative instrumentation

David C. Fritts[1], P.-Dominique Pautet[2], Katrina Bossert[1], Michael J. Taylor[2], Bifford P. Williams[1], Hiroyuki Iimura[1], Tao Yuan[2], Nicholas J. Mitchell[3], and Gunter Stober[4]

[1]GATS, Boulder Division, Boulder, Colorado, USA, [2]Center for Atmospheric and Space Science, Utah State University, Logan, Utah, USA, [3]Centre for Space, Atmospheric and Oceanic Science, University of Bath, Bath, UK, [4]Institute for Atmospheric Physics, Kühlungsborn, Germany

Abstract An Advanced Mesosphere Temperature Mapper and other instruments at the Arctic Lidar Observatory for Middle Atmosphere Research in Norway (69.3°N) and at Logan and Bear Lake Observatory in Utah (42°N) are used to demonstrate a new method for quantifying gravity wave (GW) pseudo-momentum fluxes accompanying spatially and temporally localized GW packets. The method improves on previous airglow techniques by employing direct characterization of the GW temperature perturbations averaged over the OH airglow layer and correlative wind and temperature measurements to define the intrinsic GW properties with high confidence. These methods are applied to two events, each of which involves superpositions of GWs having various scales and character. In each case, small-scale GWs were found to achieve transient, but very large, momentum fluxes with magnitudes varying from ~60 to 940 $m^2 s^{-2}$, which are ~1–2 decades larger than mean values. Quantification of the spatial and temporal variations of GW amplitudes and pseudo-momentum fluxes may also enable assessments of the total pseudo-momentum accompanying individual GW packets and of the potential for secondary GW generation that arises from GW localization. We expect that the use of this method will yield key insights into the statistical forcing of the mesosphere and lower thermosphere by GWs, the importance of infrequent large-amplitude events, and their effects on GW spectral evolution with altitude.

1. Introduction

Gravity waves (GWs) propagating upward from sources at lower altitudes are major drivers of the circulation and structure at higher altitudes due to their pseudo-momentum (hereafter momentum) [see *McIntyre*, 1981] flux and body forces accompanying its divergence. Influences of GW momentum transport are especially significant in the mesosphere and lower thermosphere (MLT), where they account for the closure of the mesospheric jets, the GW-induced residual circulation from the summer to the winter mesosphere, and the corresponding thermal structure of the summer and winter polar mesospheres [*Fritts and Alexander*, 2003].

The character of GW forcing of the MLT remains largely unknown, however, as systematic global measurements able to quantify all of the relevant scales are not yet possible. While the major sources are known qualitatively, the contributions of GW filtering, interactions, spectral evolution, source intermittency, and GW localization are poorly understood at this time. Multiple observational and modeling studies at altitudes from the lower troposphere to the MLT suggest that GWs having relatively high frequencies and small horizontal scales contribute preferentially to vertical transport of horizontal momentum [e.g., *Lilly and Kennedy*, 1973; *Vincent and Reid*, 1983; *Fritts and Vincent*, 1987; *Tsuda et al.*, 1990; *Nastrom and Fritts*, 1992; *Pfister et al.*, 1993; *Nakamura et al.*, 1999; *Walterscheid et al.*, 1999; *Lane et al.*, 2001; *Yamada et al.*, 2001; *Fritts et al.*, 2002; *Horinouchi et al.*, 2002; *Kim et al.*, 2003; *Fritts and Alexander*, 2003; *Smith et al.*, 2008; *Plougonven et al.*, 2008, 2013; *Hertzog et al.*, 2008, 2012; *Smith et al.*, 2009; *Yue et al.*, 2009].

Airglow imagers, in particular, provide important information on GW horizontal scales, propagation directions, phase speeds, localization, intermittency, sources, and instability evolutions [e.g., *Taylor and Hapgood*, 1988; *Swenson and Mende*, 1994; *Taylor et al.*, 1995, 1997; *Hecht et al.*, 1997, 2000; *Yamada et al.*, 2001; *Fritts et al.*, 2002; *Ejiri et al.*, 2003; *Nakamura et al.*, 2003; *Suzuki et al.*, 2004; *Li et al.*, 2005, 2007; *Wrasse et al.*, 2006; *Xu et al.*, 2006; *Simkhada et al.*, 2009; *Yue et al.*, 2009]. Airglow measurements have also been

employed to estimate GW momentum fluxes, given their unique sensitivity to the smaller horizontal GW scales believed to account for the dominant fluxes in the MLT [e.g., *Swenson and Liu*, 1998; *Swenson et al*., 1999; *Fritts et al*., 2002; *Tang et al*., 2002, 2005a, 2005b; *Espy et al*., 2004a, 2004b, 2006; *Suzuki et al*., 2007]. However, traditional imagers are limited by measuring only airglow intensity at one or several deep airglow layers (typical layer full width at half maximum, FWHM ~7 km) centered from ~85 to 95 km. This imposes uncertainties in estimates of GW amplitudes and even larger uncertainties in estimates of GW momentum fluxes because the Krassovsky ratio of airglow intensity to temperature perturbations, $\eta = (I'/I)/(T'/T)$, exhibits significant variability at a given GW period (by factors of ~2–5) [e.g., *Taori and Taylor*, 2006, and references therein]. This is because the intensity fluctuations depend on temperature, pressure, and species chemistry, while the GW momentum fluxes vary as $(T'/T)^2 = (I'/I)^2/\eta^2$ [e.g., *Swenson and Liu*, 1998; *Vargas et al*., 2007, also see section 4 below]. Hence, GW momentum flux estimates relying on airglow intensity measurements may be uncertain by factors of ~3–10 or more.

An alternative to the use of airglow intensity fluctuations for GW momentum flux estimates is two-dimensional (2-D) images of the OH airglow temperature fields obtained with Mesosphere Temperature Mappers as developed by Utah State University. Several of these are now in operation at the Arctic Lidar Observatory for Middle Atmosphere Research (ALOMAR, 69.3°N) in Norway in winter, at Logan, Utah (41.7°N) in summer, at the Andes Lidar Observatory (30.3°S) in Chile, and at South Pole [*Pautet et al*., 2014].

The new Advanced Mesospheric Temperature Mappers (AMTMs) offer a far more quantitative means of estimating GW momentum fluxes at multiple GW spatial scales because they avoid the uncertainties of inferring T'/T from I'/I. They also can further reduce uncertainties under the following conditions: (1) the vertical profiles of horizontal wind (and preferably temperature) are measured with collocated lidars and/or radars, (2) these profiles allow one to distinguish between vertically propagating and evanescent (or ducted) GWs, and (3) the GWs have sufficiently large vertical wavelengths that there is little reduction in the GW temperature amplitude due to phase cancelation across the airglow layer. In such cases, we expect estimates of GW momentum fluxes to be quite precise because all of the GW intrinsic properties and the wind and temperature amplitudes can be computed directly. An additional, and large, benefit that we will exploit here is the measurement of temperature (thus also estimates of horizontal and vertical velocity) perturbations as 2-D temperature maps allowing determination of the spatial extent and duration of regions of significant momentum flux within the AMTM field of view (FOV). This is expected to be a major benefit because we currently have a very limited understanding of the spatial extents of GW forcing events in the MLT. Yet such information is critically important, given the expectation that spatially and temporally localized events must excite additional GWs that may then propagate to much higher altitudes [*Vadas and Fritts*, 2001, 2002]. Additionally, momentum deposition statistics (including spatial and temporal intermittency) and secondary GW radiation are likely key to posing new and improved GW parameterization schemes for weather and climate prediction models.

This paper is organized as follows. Section 2 discusses (1) the dependence of GW momentum fluxes on AMTM temperatures, measured and inferred GW parameters, and environmental wind and temperature profiles, (2) the influences of AMTM GW phase averaging, and (3) quantification of GW momentum fluxes for extended and spatially localized GW packets. Applications of these methods to two GW packets observed by the AMTM and other instruments at Logan and Bear Lake Observatory (BLO) in Utah and at ALOMAR are discussed in section 3. A discussion of these results is provided in section 4. Our summary and conclusions are provided in section 5.

2. Determination of GW Parameters and Momentum Fluxes

2.1. Dependence on GW and Mean Parameters

We assume GW propagation in the (x,z) plane without loss of generality and employ the linear 2-D perturbation equations describing conservation of momentum, mass, and energy and the definition of potential temperature, $\theta = (p/\rho R)(p_0/p)^{\kappa}$, from *Fritts and Alexander* [2003] for deep GWs in an atmosphere having a mean wind U_h along the GW propagation direction. Also, assuming the GWs of interest to have intrinsic frequencies $\gg f$ (the Coriolis frequency), these equations may be written as

$$du'/dt + w'\partial U_h/\partial z + \partial(p'/\rho_0)/\partial x = 0 \quad (1)$$

$$dw'/dt + \partial(p'/\rho_0)/\partial z - (1/H)(p'/\rho_0) + g\rho'/\rho_0 = 0 \quad (2)$$

$$d(\rho'/\rho_0)/dt + \partial u'/\partial x + \partial w'/\partial z - w'/H = 0 \quad (3)$$

$$d(\theta'/\theta_0)/dt + w'(N^2/g) = 0 \quad (4)$$

$$(\theta'/\theta_0) = (1/{c_s}^2)(p'/\rho_0) - (\rho'/\rho_0) \quad (5)$$

Here u', w', p', ρ', and θ' are the perturbation horizontal and vertical velocities in the plane of GW propagation, pressure, density, and potential temperature, g is gravity, $\kappa = R/c_p = 2/7$, $d/dt = \partial/\partial t + U_h\,\partial/\partial x$, p_0, ρ_0, θ_0, the density scale height H, and the static stability $N^2 = d\theta_0/dz$ (buoyancy frequency $N = 2\pi/T_b$ with T_b is the buoyancy period) are mean quantities that may vary in altitude. Assuming GW perturbations vary as

$$u', w', \theta'/\theta_0, p'/\rho_0, \text{ and } \rho'/\rho_0 \sim \exp[i(kx + mz - \omega t) + z/2H] \quad (6)$$

and neglecting shear and curvature terms in the mean wind, $\partial U_h/\partial z = \partial^2 U_h/\partial z^2 \sim 0$, a GW with wave number components (k, m) and observed frequency $\omega = kc$ and phase speed c yields

$$-i\omega_i u' + ikp'/\rho_0 = 0 \quad (7)$$

$$-i\omega_i w' + (im - 1/2H)p'/\rho_0 = -g\rho'/\rho_0 \quad (8)$$

$$-i\omega_i \rho'/\rho_0 + iku' + (im - 1/2H)w' = 0 \quad (9)$$

$$-i\omega_i \theta'/\theta_0 + (N^2/g)w' = 0 \quad (10)$$

$$\theta'/\theta_0 = (1/{c_s}^2)p'/\rho_0 - \rho'/\rho_0 \quad (11)$$

Here $\omega_i = kc_i = k(c - U_h)$ is the intrinsic frequency and c_i is the GW intrinsic phase speed.

These equations yield the approximate GW dispersion relation for deep GWs given by

$$m^2 = k^2(N^2/{\omega_i}^2 - 1) - 1/4H^2 \quad (12)$$

which is identical to the anelastic and compressible forms under the above assumptions [*Fritts and Alexander*, 2003; *Lund and Fritts*, 2012]. We note, for completeness, that the relations among GW perturbations, k, m, and ω_i in equations (7)–(12) would be considerably more complex had we retained mean wind shear and curvature terms [*Nappo*, 2002]. However, this would have rendered them nearly unusable for our purposes here, given our inability to define all of the GW and mean flow terms quantitatively. In particular, while the first term on the right-hand side (RHS) of equation (12) is usually by far the dominant term, the second term on the RHS, $1/4H^2$, is often smaller than the neglected shear and curvature terms in complex environments. Indeed, these same reservations apply to all efforts to assess GW propagation and momentum fluxes, whether or not they have been included in the derived equations. Hence, when the $1/4H^2$ term becomes important, then other neglected terms should likely also be considered.

In the large majority of the applications envisioned in this paper, GWs will have sufficiently small vertical wavelengths $\lambda_z = 2\pi/m$ that the last term in equation (12) is negligible. This occurs for ${\lambda_z}^2 \ll (4\pi H)^2$. With $4\pi H \sim 75$ km for typical MLT conditions, this implies GWs having $\lambda_z \sim 25$ km or less will satisfy this condition. The other neglected terms can likewise be assumed to be negligible for local assessments of amplitudes and momentum fluxes for GWs that appear to have a relatively uniform λ_z with altitude, even if this depth is less than λ_z.

To assess GW momentum fluxes as quantitatively as possible, we need to relate T' measurements by AMTMs and lidars to the GW quantities in equations (7)–(11). For this purpose, we employ the linearized form of the ideal gas law [*Lund and Fritts*, 2012], for temperature perturbations, T', and mean temperature $T_0(z)$ that in general varies with altitude, given by

$$T'/T_0 = p'/p_0 - \rho'/\rho_0 = \theta'/\theta_0 + (p'/p_0)(1 - p_0/\rho_0 gH) \quad (13)$$

Using equation (11), the pressure scale height defined as $H_p = RT/g$, and $\gamma = C_p/C_v$, this may be rewritten as

$$T'/T_0 = \theta'/\theta_0 + \gamma(\theta'/\theta_0 + \rho'/\rho_0)(1 - H_p/H) \quad (14)$$

Thus, for an isothermal atmosphere with $T_0(z)$ constant, $H_p = H$, and equation (14) simplifies to

$$T'/T_0 = \theta'/\theta_0 \quad (15)$$

More generally, for $T_0(z) \neq 0$ and lapse rate $\Gamma = -dT/dz$, the terms in the ideal gas law can be expanded as Taylor series for small z to yield

$$H - H_p = HH_p\Gamma/T_0 + \text{ higher order terms} \tag{16}$$

For T_0 ~200 K, H and H_p ~6 km, and $|\Gamma|$ ~2 K/km, which are typical of, or larger than, mean values in the MLT, equation (16) implies differences between $H - H_p$ of <0.4 km. Thus, equation (14) implies that

$$T'/T_0 = \theta'/\theta_0 \pm 0.1\ (\theta'/\theta_0 + \rho'/\rho_0) \sim \theta'/\theta_0 \tag{17}$$

This is consistent with the relation inferred by assuming that the GWs of interest have $c_i \ll c_s$ and are thus relatively incompressible. This further implies that $-i\omega_i\rho'/\rho_0$ in equation (9) and ${c_s}^2$ in equation (11) can also be neglected, yielding the equations

$$iku' + (im - 1/2H)w' = 0 \tag{18}$$

$$T'/T_0 = \theta'/\theta_0 = -\rho'/\rho_0 \tag{19}$$

with small uncertainties, except when Γ departs significantly from its mean value.

Finally, for λ_z <25 km and k/m <0 for upward propagation, equations (10), (11), and (19) yield

$$(T'/T_0) = (\theta'/\theta_0) = -\,\mathrm{i}(Nu'/g)\left(1 - \omega_i^2/N^2\right)^{-1/2} \tag{20}$$

$$< u'w' > = \left(g^2\omega_i/2N^3\right)\left(1 - \omega_i^2/N^2\right)^{1/2}(T'/T_0)^2 \tag{21}$$

For a spatially localized GW packet, $T'(x,y)$ will vary with horizontal position and its spatial extent will define the approximate scale of the region influenced by GW momentum transport and deposition where GW dissipation occurs.

2.2. Influences of Phase Averaging Within the OH Layer

Because the OH airglow layer has a typical FWHM intensity (or brightness) of ~7 km [*Baker and Stair*, 1988], measured temperatures will be less than the maximum values at the peak intensity for GWs for which the layer depth is a significant fraction of λ_z. It is usually assumed that the intensity can be approximated as a Gaussian distribution in the vertical

$$I(z) = I_0 \exp\left[-(z - z_0)^2/2{\sigma_z}^2\right] \tag{22}$$

where I_0 is the peak intensity, z_0 is the center of the OH layer, $\sigma_z = z_{FWHM}/2(2\ln 2)^{1/2}$, and z_{FWHM} is the FWHM airglow layer width, typically ~7 km, such that the measured temperature perturbation is given approximately by

$$< T' > = \int T'(z)I(z)dz / \int I(z)dz \tag{23}$$

The phase of the GW yielding the largest $< T' >$ will occur where the maximum (or minimum) $T'(z) = T_0'\cos[(2\pi/\lambda_z)(z - z_0)]$ occurs at $z = z_0 \pm n\lambda_z/2$, with n an integer. This yields a ratio of measured to true temperature fluctuations given by

$$C = < T' > /T'(z_0) = \exp\left(-\pi^2 {z_{FWHM}}^2/4\ln 2{\lambda_z}^2\right) = \exp\left(-3.56{z_{FWHM}}^2/{\lambda_z}^2\right) \tag{24}$$

Thus, C ~0.41, 0.67, and 0.80 for λ_z/z_{FWHM} = 2, 3, and 4, respectively, and significant phase averaging (and insensitivity to T') occurs only for λ_z/z_{FWHM} less than ~3. Assuming correlative lidar or radar measurements enable an estimate of λ_z, the effect of phase averaging on the momentum flux estimate can be included by rewriting equation (21) as

$$< u_h'w' > = \left(g^2\omega_i/2N^3\right)\left(1 - \omega_i^2/N^2\right)^{1/2}(< T' > /T_0)^2/C^2 \tag{25}$$

where $< T' > (x, y)$ is the GW amplitude measured by the AMTM and C is a function of λ_z/z_{FWHM} given by equation (24).

In cases where there is significant large-scale wind shear expected to impact GW vertical structure, a steady, linear GW will have a vertical velocity given by a Frobenius expansion [*Booker and Bretherton*, 1967] with a leading term that varies as

$$w'(z) \sim \delta_z{}^{1/2} \exp(\pm i\mu \ln \delta z) \tag{26}$$

Here $\delta z = z - z_c$, z_c denotes the height of a critical level for the GW (typically above an upward propagating GW packet), we assume a uniform shear in the vicinity of z_c, a local vertical wave number $\mu = (Ri - ¼)^{1/2}$, and a corresponding local λ_z that decreases as δz, where Ri is the local Richardson number, $Ri = N^2/(dU/dz)^2$, and dU/dz is the mean wind shear. This implies a corresponding $u'(z) \sim \delta z^{-1/2} \exp(\pm i\mu \ln \delta z)$, such that the momentum flux remains constant with altitude in the absence of dissipation. Far from a critical level, GW structure varies only slightly from a uniform λ_z, and momentum flux estimates provided by equations (24) and (25) are expected to be good approximations. However, proximity to z_c (with $\delta z \sim \lambda_z$ or less) will cause decreasing λ_z, increasing phase cancelation within the airglow layer, and reductions in $< T' >$ relative to T', requiring a numerical solution of equation (23) to properly estimate the GW momentum flux. In practice, a GW cannot avoid dissipation (and sharply reduced momentum flux) due to instability and/or viscosity and thermal diffusivity as z_c is approached, though GW momentum transport and "self acceleration" may alter the local mean flow and the GW phase speed itself [*Sutherland*, 2001, 2006; *Fritts and Lund*, 2011]. Thus, the GW T' must be small where significant phase averaging occurs near z_c. For additional discussion of the implications of critical level dynamics, the interested reader is referred to *Booker and Bretherton* [1967] and *Fritts* [1984].

2.3. Methodology

As noted above, multiple observations suggest that the majority of GW momentum flux from the lower atmosphere into the MLT accompanies GWs exhibiting small horizontal wavelengths, λ_h ~100 km or less, and high observed (and intrinsic) frequencies, ω and ω_i, with typical observed periods, $T_{obs} = 2\pi/\omega$ ~1 h or less [e.g., *Nastrom and Fritts,* 1992; *Fritts and Alexander*, 2003, and references above]. This implies that AMTM sensitivity to GWs having λ_h ~10 to 100 km has the potential to quantify the majority of GW momentum fluxes at the OH airglow altitude (e.g., the AMTM FOVs at ~87 km at ALOMAR and Logan are 180 × 144 km), whether these GWs are localized within the AMTM FOV or have larger extents.

GWs are typically localized in space and time, yielding a packet having a 2-D $< T' >(x,y)$ field (hereafter using T' in place of $< T' >$ in this section for simplicity) at the airglow layer. When GW packet scales exceed the FOV of the AMTM, wavefield fits will be performed for the entire FOV and optimized to define a "best fit" monochromatic GW for a horizontal wavelength, λ_h, propagation direction, ϕ, and temperature amplitude, T' (by minimizing the root-mean-square T' error). As most GWs have spatial extents of several λ_h, a full FOV GW fit is more likely for GWs having larger spatial scales. Optimal fits to the keograms and 2-D FFTs can also provide these estimates, depending on the GW spatial scales (see section 3 below).

When GW packets are localized within the AMTM FOV in one or both dimensions at one time, or via their signatures in N-S and/or E-W keograms (determined from temporal sampling of orthogonal AMTM pixel rows) as they propagate through the FOV, we expect them to exhibit central maxima and roughly elliptical forms with major and minor axes along or across the GW packets. In such cases, it is possible to approximate the $T'(x,y)$ field with a simple spatial form enabling a quantitative estimate of the momentum flux distribution in space and time. Such information is valuable for assessing the GW packet scales and their intermittency of the forcing accompanying GW dissipation and momentum transport.

In most cases, AMTM, airglow, and other measurements indicate that isolated, individual GW packets occur very infrequently. Thus, for general and/or automated GW momentum flux estimates, we expect to employ both 2-D fast Fourier transforms (FFTs) and full FOV or local wavefield fits to quantify the key parameters, e.g., λ_h, ϕ, observed and intrinsic horizontal phase speeds, c and c_i, and T', for individual GW packets. These more complex environments will lead to greater uncertainties in fits and GW parameters. Here, however, we will confine our attention to cases for which defining a single GW packet is relatively straightforward. A more complete assessment of uncertainties accompanying superposed GWs, the presence of quasi-2-D ducted GWs and/or Kelvin-Helmholtz instabilities (KHI), and possible 3-D structures accompanying KH billow breakdown, GW breaking, and/or 3-D turbulence, will be addressed separately.

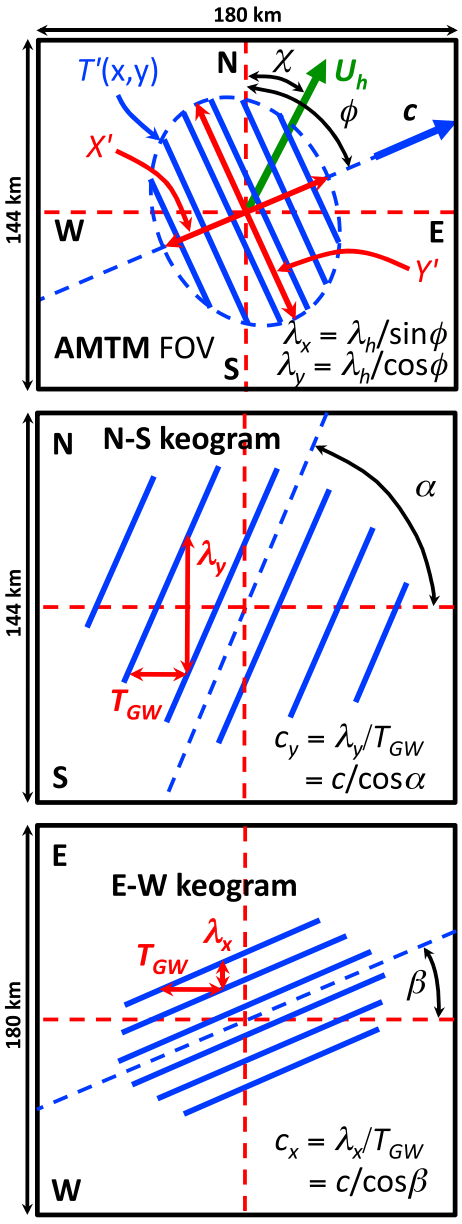

Figure 1. (top) Example GW packet geometry seen by the AMTM relating GW scales and orientation. (middle and bottom) Examples of N-S and E-W keograms and the relations between apparent wavelengths and phase speeds and the observed GW period and phase speed.

In order to estimate the spatial extent of a GW packet, we assume either a uniform, Gaussian, or half-cosine distribution of $T'(x',y')$ to quantify GW packet characteristics and simplify our GW momentum flux and total momentum estimation procedures. For GW packets within the AMTM FOV, we assume a maximum amplitude $T' = T_0'$ at (x'_0,y'_0) and along-track and cross-track FWHM dimensions of X' and Y' (with x' increasing along the GW propagation direction), we can approximate the spatial variations of $T'(x',y')$ as either

$$T'(x',y') = T_0' \exp\left\{-4\ln 2\left[(x'-x'_0)^2/X'^2 + (y'-y'_0)^2/Y'^2\right]\right\} \quad (27)$$

or

$$T'(x',y') = T_0' \cos[2\pi(x'-x'_0)/3X'] \cos[2\pi(y'-y'_0)/3Y'] \quad (28)$$

where equation (28) assumes a fit for $|x'-x'_0| \le 3X'/4$ and $|y'-y'_0| \le 3Y'/4$. We assume GW packet coordinates (x',y') with x' aligned at angle ϕ east of north (see Figure 1, top) and geographic coordinates with x to the east. With this convention, the relations between the GW packet λ_h, ϕ, c, and the apparent zonal (x) and meridional (y) wavelengths, $\lambda_x = 2\pi/k_x$ and $\lambda_y = 2\pi/k_y$, and phase speeds, $c_x = \lambda_x/T_{GW}$ and $c_y = \lambda_y/T_{GW}$ as they would appear in the AMTM image and the N-S and E-W keograms are shown in Figure 1. Here T_{GW} is the GW period and $k_h^2 = k_x^2 + k_y^2$ implies that $1/c^2 = 1/c_x^2 + 1/c_y^2$.

2.4. Instrumentation

Our momentum flux assessments in this paper employ MF or meteor radar, sodium lidar, and AMTM measurements to define the temperature and horizontal velocity fields and the ~87 km temperature maps at BLO and ALOMAR. The spatial and temporal resolutions of these instruments employed for this study are shown in Table 1.

3. Momentum Flux Estimates

3.1. Event 1: Observations at Logan and BLO, 6 June 2013

N-S and E-W OH (3,1) temperature keograms showing a number of GW responses from ~4:30 to 11 UT on 6 June 2013 are shown in Figure 2 (top panel). Keograms are generated separately from the AMTM brightness and temperature time series data by sequencing orthogonal pixel rows and columns through each image to create N-S

Table 1. Spatial and Temporal Resolution of the Instruments at BLO and ALOMAR Used in This Study

Instrument and Location	Vertical Resolution	Horizontal Resolution	Temporal Resolution
AMTM, BLO and ALOMAR	~7 km[a]	0.56 km, (320 × 256) pixels	35 s
Na lidar, BLO	140 m	--	5 min
Meteor radar, BLO	3 km	--	1 h
Na lidar, ALOMAR	1.13 km	--	10 min
SAURA radar, ALOMAR	1 km	--	7.5 min

[a]The AMTM averages over the OH layer depth.

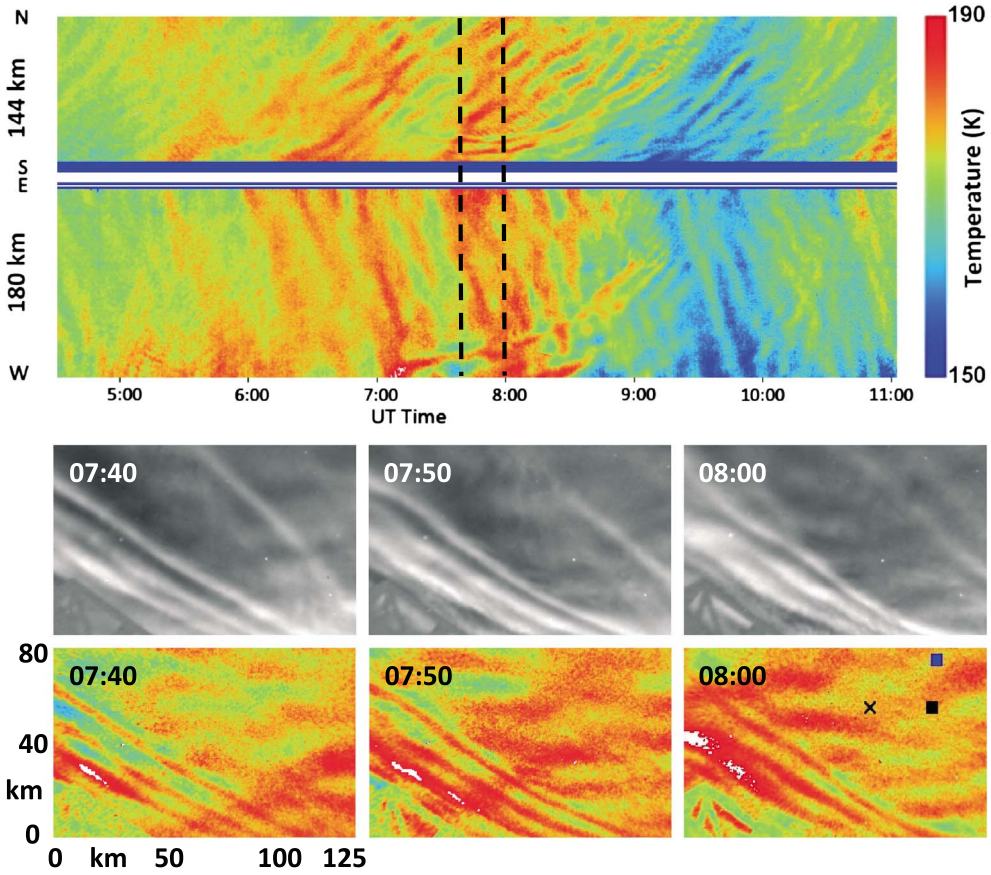

Figure 2. (top) 6.5 h segments of the N-S and E-W keograms for the Event 1 GW observed over Logan, Utah on 6 June 2013. The GW of interest is that showing very little phase motion during the interval examined, from 7:40 to 8:00 UT shown with dashed lines. (bottom) AMTM brightness and temperature fields at 10 min intervals spanning the times of interest. Keograms were computed from the central pixel row or column of the detector for each direction. Figure 2 (bottom right) also shows the locations of the GW relative to Logan ("cross"), BLO (blue square), and the east beam of the USU Na lidar at 87 km (black square). Spatial scales of the images are shown in Figure 2 (bottom left).

and E-W summary plots of the nocturnal GW activity. The keograms reveal a superposition of larger- and smaller-scale GW responses having observed periods ranging from ~20 min to 6 h or longer. Our focus here is on the interval within the dashed vertical lines in the keograms, which is a subset of a longer interval exhibiting a superposition of two GW fields extending from ~7 to 9 UT. Zoomed images of this event in the AMTM emission $I(x,y)$ and $T(x,y)$ fields (north and east up and to the right, respectively) are shown at 10 min intervals in Figure 2 (bottom panels). The lower images reveal both (1) a larger-scale GW propagating toward the NNW with λ_h ~21 km, $\phi \sim -20°$, and c ~30 m s^{-1} occupying most of the AMTM FOV and (2) a smaller-scale GW propagating toward the NE with λ_h ~12.5 km, ϕ ~40°, and c increasing from ~0 to ~10 m s^{-1} confined to the south and west AMTM FOV at these times.

The larger-scale GW spans the AMTM FOV and appears to be a ducted GW, based on correlative wind and temperature measurements and its persistence for ~5 h. Winds in the plane of GW propagation exhibit almost no shear, are ~70 m s^{-1} opposite to the propagation direction at ~87 km (not shown), and imply a large intrinsic phase speed of ~100 m s^{-1} and an implied intrinsic frequency of ω_i ~0.03 s^{-1}. This is marginally below the maximum N near 88 km of ~0.039 s^{-1} but is substantially above the smaller N ~0.017 s^{-1} inferred at higher and lower altitudes (see the discussion of Figure 3 below). In contrast, the smaller-scale GW (which we label Event 1) is more localized in space, more transient, and more dynamically active. See, for example, the indications of phase speed accelerations accompanying the later stages of Event 1 (~8 to 9 UT) at the lower edges of both keograms. Because Event 1 is confined to the lower left portion of the AMTM FOV, however, its maximum amplitude is not seen in either keogram. Hence, we rely largely on individual AMTM images for its characterization. Key features of the Event 1 GW packet include the following:

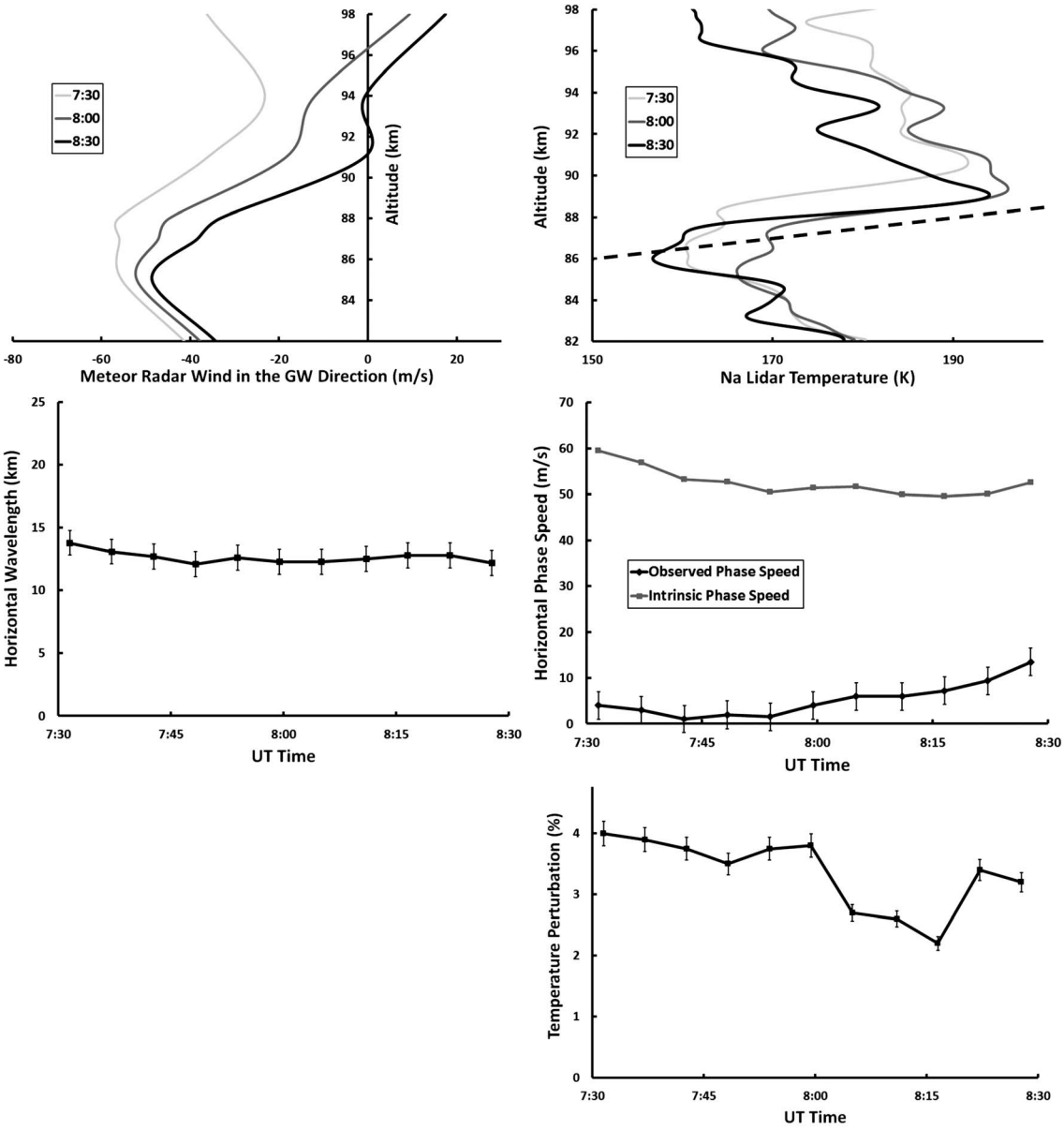

Figure 3. (top) Meteor radar winds in the plane of GW propagation from 1 h averages centered at 7:30 and 8:30 UT (left) and interpolated to 8:00 UT, and 30 min Na lidar temperature profiles centered at 7:30, 8:00, and 8:30 UT (right). (middle and bottom) AMTM estimates for the GW λ_h, c, c_i, and $< T'/T >$ at ~4.5 min intervals spanning the times of interest. Error bars on the line plots in the bottom three panels show the uncertainties for 30 s estimates. Error bars are not shown for c_i because measured U uncertainties are not known. Variations at longer time scales represent geophysical variability.

1. it arises in place, rather than propagating into the FOV from the SW, beginning ~7:20 UT, so it can only have propagated into the airglow layer from below;
2. it appears to have a very restricted extent along its direction of propagation at early times, as only ~4 cycles spanning ~50 km are visible prior to 8 UT;
3. successive images reveal additional phase fronts, with decreasing T', thereafter, and
4. the GW exhibits strong instability at its leading edge beginning ~9 UT (not shown), providing further evidence of amplitude growth with time and altitude.

To diagnose the Event 1 GW packet character in greater detail, we employ the USU Na lidar located at Logan, Utah, and the meteor radar located at BLO, separated by ~40 km. The $T(z)$ profiles were obtained in the lidar east beam, which is ~30 km east of Logan at the OH layer. The lidar (Logan), lidar east beam, and meteor radar (BLO) locations are shown with the "X" and the black and blue squares, respectively, in Figure 2

Table 2. Measured and Inferred GW Parameters for Event 1[a]

T_{GW}	ϕ (From North)	T' (K)	c (m s^{-1})	c_i (m s^{-1})	λ_h (km)	λ_z (km)	u_h' (m s^{-1})	w' (m s^{-1})	$\lvert dT'/dz \rvert$ (K km^{-1})	$<u_h'w'>$ m^2 s^{-2}
70 min	~40° (NE)	9.1	~3	52	12.5	21.7	8.5	~14.7	~2	~62

[a]Uncertainties greater than ~10% are indicated by a "~".

(bottom right panel). An OH profile obtained by the SABER instrument aboard the Thermosphere Ionosphere Mesosphere Energetics and Dynamics satellite was also available at 12:53 UT ~600 km to the ESE. This shows an OH layer with z_{FWHM} ~7 km, confirming our assumption above.

Shown in Figure 3 are horizontal winds in the plane of GW propagation, $U_h(z)$, for 1 h averages at 30 min intervals measured with the meteor radar, $T(z)$ at 30 min intervals measured with the Na lidar, λ_h, c, and $<T'>$ measured with the AMTM throughout Event 1, and the inferred $c_i = (c - U_h)$ assuming the OH layer was centered at ~87 km from 7 to 8 UT. $<T'>$ was estimated from the power in the 2-D Fourier transform for a localized domain within the GW field. Typical uncertainties in AMTM measurements of λ_h, c, $<T'>$, and ϕ are ~3, 3, and 5% and ~1° for individual 30 s estimates and ~1, 1, and 2% and <1° for a 5 min (10-sample) average.

The lidar profiles indicate a maximum dT/dz ~20 K km^{-1} (dashed line, upper right panel) at 7:30–8:30 UT, implying a maximum N ~0.039 s^{-1}. There is significant uncertainty in the true mean $T(z)$ profiles for Event 1, however, as the profiles shown also include lower frequency GWs (note the 5 h or longer-period GW contributing ~15 K fluctuations in the keograms). These structures also must yield horizontal variations in the $T(z)$ structure and altitude of maximum N^2 at the site of Event 1 relative to the location of the lidar $T(z)$. For reference, the maximum amplitude of the GW in Event 1 is near the left edge of Figure 2 (bottom right panel), ~120 km from the $U_h(z)$ and $T(z)$ profiles to the east and NE of Logan. The mean temperature gradient over the airglow layer is much less, with dT/dz ~5–10 K km^{-1} (we estimate an ~25–30% uncertainty in N^2) and a corresponding range of N ~0.028–0.032 s^{-1}, depending on the actual airglow altitude during the BLO observations.

The various measurements imply best estimates for the GW parameters at the event times from 7:40 to 8:00 UT of λ_h ~12.5 km, U_h ~ −49 m s^{-1}, c ~3 m s^{-1}, $c_i = (c - U_h)$ ~52 m s^{-1}, and $<T'>/T_0$ ~ 3.7%. Given $\omega_i = k_h c_i$ ~0.026 s^{-1}, N ~0.03 s^{-1}, and z_{FWHM} ~7 km, equations (12), (24), and (25) imply λ_z ~1.74λ_h ~21.7 km, C^2 ~ 0.48, u_h' = 8.5 m s^{-1}, w' = 14.7 m s^{-1}, and $<u_h'w'>$ ~62 m^2 s^{-2}. These parameters are summarized in Table 2 for convenience.

For reference, the smaller and larger limits of likely N ~0.028 and 0.032 s^{-1} yield estimates of $<u_h'w'>$ ~47 and 86 m^2 s^{-2}, respectively. Additionally, a 10% increase in z_{FWHM} changes the $<u_h'w'>$ estimate by ~7%. These various estimates imply a cumulative uncertainty of ~40% about the central value, in the absence of direct measurements of local dT/dz and z_{FWHM}. The range of $<u_h'w'>$ estimates is ~5–10 times those typically measured by radars or inferred from middle atmosphere general circulation models (GCMs) at ~87 km [e.g., *Fritts and Alexander*, 2003]. Finally, we employ the spatial distribution given by equation (28) to approximate the dimensions of this GW packet. These yield an along-track FWHM packet width estimate of X' ~40 km. The cross-track packet width was much larger. These results are discussed in relation to previous studies and more general MLT dynamics in section 4.

3.2. Event 2: Observations at ALOMAR, 28 January 2014

An overview of Event 2 is provided with N-S and E-W keograms spanning 12 h, zoomed and 0.5–2 h band-passed keograms spanning 2.5 h, and six OH airglow $T(x,y)$ fields at 5 min intervals in Figure 4. The keograms are shown for two intervals: 12 h spanning an anticipated semidiurnal tide period and 2.5 h zooming in on the medium- and smaller-scale GWs at later times. As in Event 1, the keograms exhibit a superposition of larger- and smaller-scale GW, tidal, and/or longer-period responses. The keograms spanning 12 h suggest a semidiurnal (SD) tide or large-scale inertia GW (IGW) having a temperature amplitude of T' ~15 K. Caution is prudent in this interpretation, however, because large-amplitude, ~12 h features are often seen at ALOMAR and other northern and southern high-latitude sites [e.g., *Williams et al.*, 2006; *Fritts et al.*, 2010]. But near ALOMAR (69°N, 15°E), the SD tide is predicted by the GSWM-09 model to be quite small at this time [*Zhang et al.*, 2010a, 2010b].

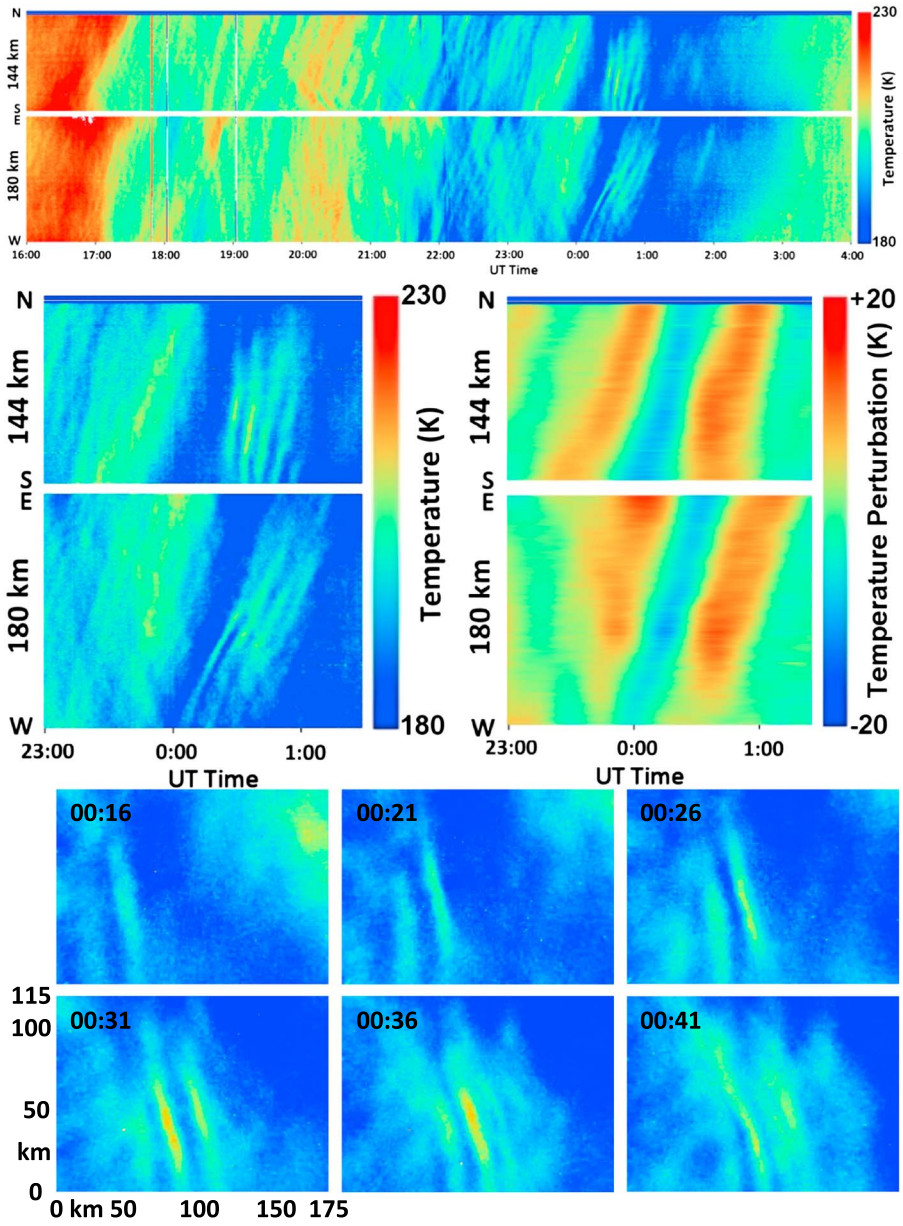

Figure 4. (top) 12 h segments of the N-S and E-W keograms for Event 2 observed over ALOMAR on 27 and 28 January 2014. Seen are apparent periods of ~12, 4, and 1–1.5 h and the Event 2 GW of ~10 min between 00 and 01 UT. (middle) Expanded view of the Event 2 GW keogram interval (left) and this same keogram with a 0.5–2 h band pass highlighting the ~1 h GW background. (bottom) AMTM temperature image sequence showing the evolution of the Event 2 GW. Note that the strongest phase front lags the GW phase speed over this interval. Times in the bottom images are in UT for comparison with the keograms. Spatial scales of the images are shown at the bottom left.

For reference, the mean January SD tide is predicted by GSWM-09 to have zonal wind and temperature amplitudes of $u' < 1$ m s^{-1} and $T' < 1$ K, respectively, at all altitudes from 80 to 100 km. The predicted February SD tide u' increases from ~4 m s^{-1} at 82 km to ~7.5 m s^{-1} at 95 km and above, but T' remains <0.5 K at the relevant altitudes. Hence, it remains uncertain whether the large ~12 h u' and T' observed at ALOMAR are SD tides that are inconsistent with GSWM-09 predictions or are instead large-amplitude IGWs having comparable periods. Additional evidence that such features may often be due to a large-scale IGW comes from the observed vertical wavelength, which for the results shown by *Williams et al.* [2006] was ~20 km, whereas the GSWM-09 SD tide estimates are ~30–40 km. Our current measurements with additional radar

Table 3. Measured and Inferred GW Parameters for Event 2[a]

T_{GW}	ϕ (From North)	T' (K)	c (m s^{-1})	c_i (m s^{-1})	λ_h (km)	λ_z (km)	u_h' (m s^{-1})	w' (m s^{-1})	dT'/dz (K km^{-1})	$<u_h'w'>$ m^2 s^{-2}
~12 h	~90° (E)	~16	~90	~90	~4000	~30	~33	~0.2	~ −3	<2
~4 h	~90° (E)	~3-5	>200	>200	>2800	large	~14	~1	~0	~5–10
~1 h	50° (NE)	~11-15	~60	~47	~200	~20	~35	~3.5	~0	~60
~10 min	70° (ENE)	19.3	45	33	24	17.6	51	~37	~6.9	~940

[a]Uncertainties greater than ~10% are indicated by a range of values or denoted by a ~.

and lidar instruments at ALOMAR to be discussed below suggest larger vertical wavelengths than observed by *Williams et al*. [2006].

The keograms in Figure 4 exhibit a number of specific features of relevance to our analysis. These include the following: (1) a decrease of the large-scale $T(x,y)$ from ~20 to 02 UT accompanying the decreasing T' phase of the ~12 h GW or SD tide, (2) apparent modulations of the large-scale $T(x,y)$ by GWs having periods of ~1 and 4 h, and (3) small-scale GWs having ~10 min periods that are visible throughout the 2.5 h keograms, which exhibit two clear, localized responses from ~23:20 to 01:20 UT.

The characteristics measured or inferred for each of the dominant wave motions observed during this interval are listed for convenience in Table 3.

Small-scale GWs during this interval (a) exhibit increasing T' amplitude modulations at an ~1 h period after ~22 UT, (b) achieve maximum T' amplitudes that are coincident with the final two ~1 h GW T' maxima, and (c) propagate primarily toward ~70°E of north after ~22:20 UT. The second of the two local GW responses occurring between ~00 and 01:20 UT is our focus in Event 2 due to its larger T' amplitude and its confinement largely within the AMTM FOV. Confinement of the GW packet within the AMTM FOV ensures that it almost certainly enters from below and exits above, as it clearly does not enter or exit through the edges of the FOV and its amplitude appears to be too large to have propagated downward from significantly higher altitudes (because it has no earlier OH airglow signature) without displaying instability at the larger amplitudes implied at higher altitudes.

Correspondence of the two GW packets occurring between 23:20 and 01:20 UT with local T' maxima of the ~1 h GW suggests that the ~1 h GW likely modulated the environment encountered by the higher-frequency GW packets, enabling or suppressing their propagation into the OH layer via local wind and/or N^2 variations. Additional evidence for such a motion is provided below. This provides important clues to the character of the Event 2 GW packet. Either an induced critical level or turning level below the OH airglow layer would seem necessary to modulate the observed Event 2 GW presence in the keograms.

If a critical level for the Event 2 GW was moving up and down across the OH layer due to variable ~1 h GW horizontal winds, its $c_i = (c - U_h)$ would be small at OH altitudes, requiring small $\omega_i = k_h(c - U_h)$, hence large m/k and small λ_z from equation (12). This would also require a small $u' \sim N/m$ or less due to instability constraints (but the lack of evidence of instability structures implies this condition is not exceeded), small implied $< T' > / T_0$ from equation (20), and long residence and propagation time scales due to a small vertical group velocity. However, the observed $< T' > / T_0$ is relatively large and the response to the ~1 h GW modulation is fairly rapid. Hence, a critical level explanation seems not defensible. Alternatively, modulation of m^2 about zero (accompanying a variable turning level altitude and GW refraction due to horizontal wind and/or N^2 modulations by the ~1 h GW) provides a far more plausible explanation, given the large observed T' of the small-scale GW packet and the rapid time scale on which responses occur.

To diagnose the Event 2 GW packet environment, structure, and dynamics in greater detail, we employ AMTM measurements to define λ_h, c, ϕ, and the maximum $< T' >$ of the GW packet as functions of time. We also employ the AMTM, the ALOMAR SAURA 3.17 MHz MF radar, and the Na lidar to characterize the mean, tidal or IGW, and the medium-frequency (~1 to 4 h period) GW background as fully as possible. The ALOMAR meteor radar confirms the larger-scale winds observed by SAURA but at coarser spatial and temporal resolutions.

SAURA zonal and meridional winds at 1 km and 7.5 min resolutions are shown versus time and altitude and as time series at 92 km in Figure 5 (left column) for the 12 h AMTM keogram interval at top in Figure 4. These reveal the expected approximate quadrature relation among u' and v' for the migrating SD tide or an IGW propagating approximately zonally. They also reveal that u' exceeds v', which we expect for a zonally

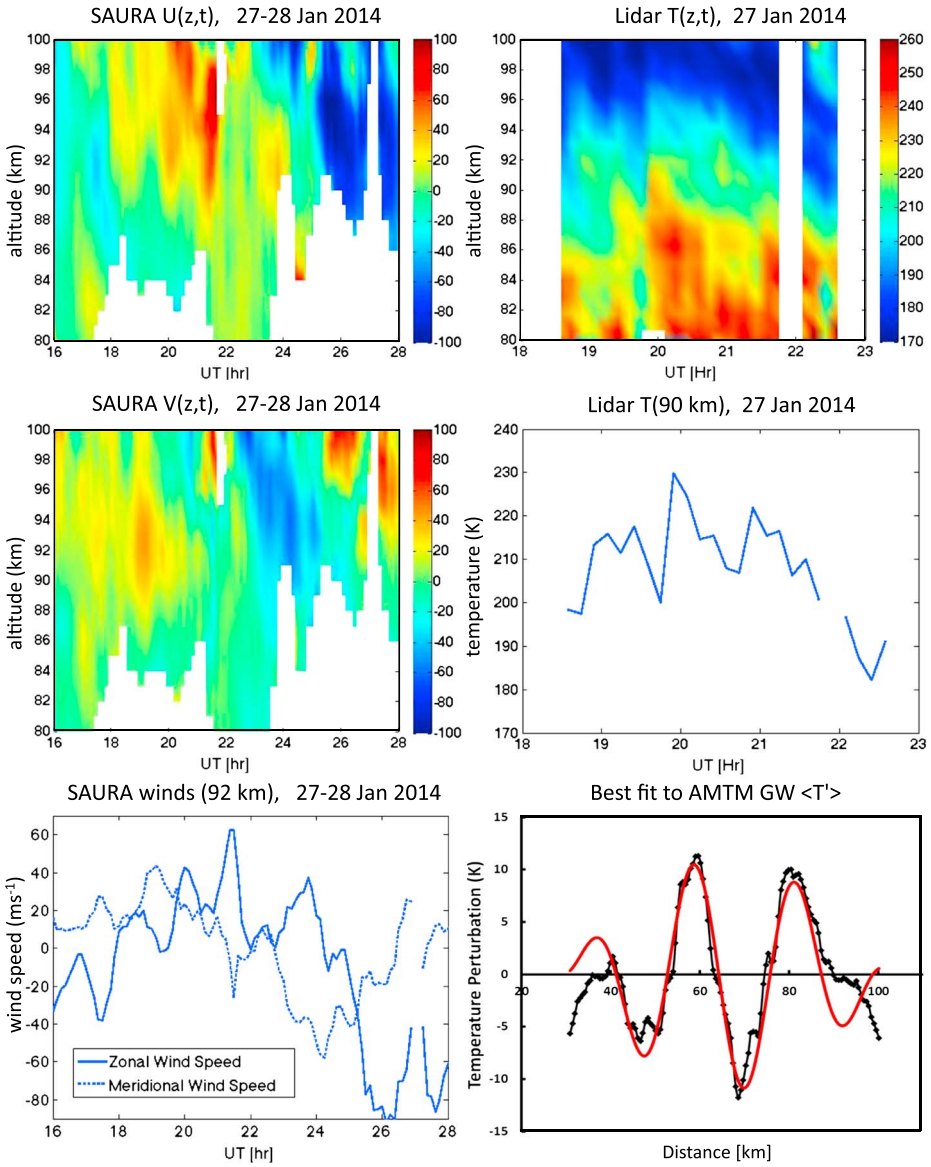

Figure 5. (left column) Zonal and meridional winds from the SAURA MF radar at 7.5 min resolution from 16 to 02 UT on 27 and 28 January 2014 from 80 to 100 km (top and middle) and at 92 km (bottom). (right column) Na lidar temperatures at 10 min resolution from 18:40 to 22:30 UT on 27 January 2014 from 80 to 100 km (top) and at 90 km (bottom). (bottom right) Best fit of a GW with λ_h = 24 km and a Gaussian amplitude envelope to the observed $< T' >$ along the GW propagation direction at 0:31 UT. The peak amplitude is 11 K.

propagating IGW, but not for the migrating SD tide. As examples, observations at high latitudes and the Canadian Middle Atmosphere Model Data Assimilation System typically exhibit migrating SD tide $v' > u'$ near winter solstice [e.g., *Baumgaertner et al*., 2006; *Murphy et al*., 2006; *Fritts et al*., 2010; *Xu et al*., 2011].

Corresponding Na lidar temperatures are shown in the same formats as the SAURA winds in Figure 5 (column), but only for 18–23 UT, because lidar operations ceased at ~22:40 UT. Comparing the wind and temperature fields suggests that the maximum zonal winds at ~20–24 UT accompany decreasing temperatures at the same altitudes. This differs from the observations at ALOMAR during the same interval in January 2003 [e.g., *Williams et al*., 2006], where large-scale zonal winds were surprisingly well correlated with the temperatures at the same altitudes. Neither correlation is consistent with a migrating SD tide, but the present phase relations are consistent with a large-scale IGW propagating largely in the zonal direction (eastward), for which u', w', and decreasing T' are largely in phase. Different correlations among the wind and

temperature fields can arise from tidal and GW superpositions. For example, the predicted GSWM-09 SD tide u' and T' fields exhibit highly variable phase differences throughout the year due to variable superpositions of the contributing modes. Likewise, GWs propagating in opposite directions will yield opposite correlations of u' with w' and T'. Together, ALOMAR wind and temperature measurements, the SD tide fields anticipated by GSWM-09, and the polarization relations for IGWs suggest that these observed large-scale ~12 h wind and temperature fields are most likely evidence of a large-scale IGW propagating largely eastward. The approximate IGW u', T', and λ_z at ~87 km inferred from the SAURA radar and Na lidar (assuming a scale height H ~6 km) are u' ~33 m s^{-1}, T' ~16 K (maximum negative $dT'/dz \sim -3$ K km^{-1}), and λ_z ~30 km (a phase descent of ~2.5 km h^{-1}), with equation (12) implying $c \sim c_i \sim N\lambda_z/2\pi$ ~90 m s^{-1} (see Table 3). Because this IGW has λ_z/λ_h ~0.007 and $v'/u' \sim \omega_i/N$ ~0.7, w' <0.3 m s^{-1}, and $< u_h'w' > <2$ m^2 s^{-2}, smaller than the expected mean (see equation (25) and Table 3).

We turn now to the medium- and higher-frequency GWs (periods of ~1–4 h) that appear to modulate the GWs at even higher frequencies and are our focus here. Evidence of these motions is apparent in the keograms in Figure 4 and in the u and T fields and/or time series shown in Figure 5. As noted above, an ~4 h GW having $< T' >$ ~3–5 K is seen throughout the 12 h keogram, and some evidence of this periodicity is also seen in u, where eastward maxima having significant vertical extent (and large λ_z) occur near ~17, 21, and 01 UT at the OH airglow layer assumed to be near 87 km. The earlier two maxima appear to be correlated with decreasing T, suggesting approximately eastward propagation, as discussed above. The observed $< T' >$ ~3–5 K, large inferred λ_z, and equations (20) and (24) imply $T' \sim < T' >$, $u' \sim (g/N)T'/T$ ~14 m s^{-1} (assuming a mean plus ~12 h GW $dT'/dz \sim -5$ K km^{-1} and $N \sim 0.0146$ s^{-1} near 01 UT, see below), and more negative, but small, total dT'/dz at this time. Additional evidence for ϕ and c for the ~4 h GW is provided by a 3–5 h band pass of the AMTM keograms (not shown). These indicate no obvious phase progression in the N-S direction, but a relatively high phase speed, c >200 m s^{-1}, to the east, confirming the inference above of large λ_z in the radar data.

Higher-frequency GWs (periods of ~1–1.5 h) are more apparent at later times (~22–01 UT) in the keograms, but are also seen throughout the 12 h u and v observations and prior to ~22 UT in the T fields displayed in Figure 5. Referring to the SAURA velocities in Figure 5, we see largely anticorrelated u' and v', with u' ~15 m s^{-1} and v' ~5–10 m s^{-1}, suggesting propagation toward the WNW or ESE from ~16 to 23 UT and generally correlated, but smaller amplitude, u' and v' from ~22 to 01 UT, implying propagation toward the NE or SW. During the earlier interval, we also see a clear superposition of GWs having differing directions of propagation in both keograms. A 0.5–2 h band pass of the keograms reveals primary propagation directions in an ~ NW-SE plane from ~16 to 19 UT, more toward the NW from ~20 to 23 UT, and strongly toward the ENE after ~23 UT, consistent with the SAURA u' and v' correlations. The latter interval, in particular, confirms the dominant NE propagation direction of the ~1 h GW inferred from the SAURA measurements from ~23 to 01 UT (see Figure 4, right middle panels).

From the AMTM keograms at ~87 km, we infer maximum $< T' >$ ~7–10 K at ~23:40 and 00:40 UT for the ~1 h GW, which implies $< T' >/T$ ~4% or greater, and u_h' ~23 m s^{-1} or greater (depending on the value of C) from equation (20). This is larger than implied by the u' and v' time series from the SAURA radar ~5 km higher, suggesting either (1) interference of GWs having similar periods and different propagation directions or (2) influences on the larger-scale velocity field by the localized ~10 min GW packets also having an ~1 h modulation to be discussed further below. There is little evidence of interference after ~00 UT, where the phase slopes in the 0.5–2 h band-passed keograms are well defined and imply c ~60 m s^{-1}. Local momentum fluxes and flow accelerations are expected to accompany localized GW packets having large amplitudes, however, and this will be assessed further below.

Referring to the SAURA velocities and the band-passed keograms in Figures 4 and 5, we see maximum eastward u' and northward v' at 92 km and nearly coincident T' maxima at ~87 km at ~23:40 and 00:40 UT. For a GW propagating toward the NE, we expect these velocities to correlate with the most rapidly decreasing T'. This suggests a roughly in-phase relation among the velocities in the GW propagation direction at ~92 km and T' at ~87 km. This implies, in turn, a maximum $du_h'/dz > 0$ at ~87 km and a crude estimate of λ_z ~20 km for an upward propagating GW with descending phase. A large λ_z estimate is also implied by both the large $< T' >$ (suggesting relatively little phase cancelation in the OH airglow layer) and the intrinsic phase speed inferred from the band-passed keograms and the estimated large-scale flow in the GW propagation direction. AMTM images spanning this period suggest a spacing of small-scale GW packets somewhat smaller

than the image diagonal, hence λ_h ~200 km. With c ~60 m s^{-1} and U_h ~13 m s^{-1} at ~00:30 UT, $c_i = (c - U_h)$ ~47 m s^{-1}, and equation (12) yields λ_z ~$2\pi c_i/N$ ~20 km for a hydrostatic GW having $N^2 >> \omega_i^2$ and local N ~0.0146 s^{-1}. These inferred velocities suggest $< u_h'w' >$ ~60 m^2 s^{-2}, which is significant relative to a mean of ~5–10 m^2 s^{-2} (see Table 3).

Limited intervals of the raw and 0.5–2 h band-passed keograms from 23 to 01:30 UT are shown in Figure 4 (left and right middle panels), respectively. These reveal a very close correspondence between the maximum T' amplitudes of two GW packets having observed periods T_{GW} ~10 min and the maximum T' of the ~1 h GW at ~23:40 and 00:40 UT. The second small-scale GW packet in the keograms at left (the Event 2 focus) propagated toward ~70°E of north from 00:15 to 01:00 UT. Expanded AMTM images of this GW packet are shown from 00:16 to 00:41 UT in Figure 4 (bottom panels). Phase progressions were estimated from both the slopes of the phase surfaces in the keograms and the maxima in the AMTM images; the peak $< T' >$ was estimated as in Event 1 from the power in the 2-D Fourier transform for a localized domain within the GW field. Finally, U_h was estimated crudely by interpolation between sparse SAURA radar measurements spanning the interval from ~23:45 to 00:45 UT. During this interval, U_h along c decreased from ~17 m s^{-1} to ~3 m s^{-1}. The resulting estimates for λ_h, c, c_i, and $< T' >/T$ from 00:15 to 00:45 UT are shown in Figure 6 (left column). Note, in particular, the decreasing c_i and the increasing $< T' >/T$ suggesting an intensifying ~10 min GW from 00:15 to 00:32 UT in an environment having $du_h/dz > 0$ at ~87 km due to the ~1 h GW structure in the u', v', and T' fields at this time.

Two additional features of the ~10 min GW packet provide further insights into its character and evolution. The first is a distinct difference in the GW packet horizontal phase and group velocities seen in the AMTM images in Figure 4. The maximum T' is seen initially at the leading phase of the GW packet (see images at 00:16–00:26 UT) but is clearly associated with the second phase at 00:31 UT and thereafter. This suggests a group velocity slower by ~10 m s^{-1}, with c ~50 m s^{-1} and c_{gh} ~40 m s^{-1} at ~00:25 UT and both decreasing with time (see Figure 6, middle left). We expect such a difference based on the GW dispersion relation, equation (12), which reveals a ratio of the intrinsic horizontal group velocity to the intrinsic horizontal phase velocity, and an identical ratio of the vertical group and phase velocities, given by |

$$\left|c_{ghi}/c_i\right| \;=\; \left|c_{gz}/c_z\right| \;=\; 1\text{–}\omega_i^2/N^2 \tag{29}$$

assuming an intrinsic reference frame in which $U_h = 0$ (and $W = 0$). For hydrostatic GWs having $m^2 >> k_h^2$ and $N^2 >> \omega_i^2$, the group and phase velocities converge. But for finite ω_i/N, equation (29) shows that c_{ghi}/c_i and c_{gz}/c_z may depart significantly from the hydrostatic limit. The ratio c_{ghi}/c_i computed from the images in Figure 4 prior to the maximum GW amplitude at 00:31 UT assuming $U_h = 0$ is ~0.75, suggesting $\omega_i/N = k_h c_i/N$ ~0.45. However, a smaller ratio (and a larger, more accurate ω_i/N) is obtained accounting for the large-scale U_h decreasing for ~18 to 12 m s^{-1} from 00:20 to 00:32 UT. This leads to estimates of c_i ~33 m s^{-1} and c_{ghi} ~21 m s^{-1} and estimates of c_{ghi}/c_i ~0.64 and ω_i/N ~0.6.

Referring to the AMTM images at 00:36 and 00:41 UT in Figure 4, we note a second interesting feature apparently arising within the phase structure of the ~10 min GW beginning at ~00:29 UT. Zoomed images of these structures in the AMTM $I(x,y)$ field are shown from 00:33 to 00:41 UT in Figure 6 (right column). This feature begins as a brightening of the leading phase of the GW packet and its initial alignment and motion are consistent with the GW phase orientation and motion until ~00:33 UT. Thereafter, it stalls suddenly (to c ~10 m s^{-1}), develops a corresponding dark phase, immediately exhibits variations along its length having scales of ~3–5 km, and appears to also initiate additional variations in brightness that are also aligned with the GW phase and have smaller spatial scales in the plane of GW propagation (see the images in Figure 6 at 00:35 UT and thereafter). For reference, the white ovals in the images in Figure 6 have $c = 0$.

The GW phase structures appear unaffected by this feature but its amplitude decreases sharply following the appearance of this feature (see the $< T' >/T$ plot in Figure 6, bottom left). We cannot say with certainty that this feature is due to the ~10 min GW or that it is an indication of instability accounting for the GW amplitude reductions thereafter. However, the apparent initiation of this feature accompanying a large GW amplitude, its rapid development of apparent instabilities at smaller spatial scales, its stalling relative to the GW phase progression, and the strong decrease in the GW amplitude thereafter are all consistent with previous high-resolution observations and modeling of GW instability dynamics. Indeed, we expect to see exactly these indications of secondary instabilities that exhibit smaller-scale 3-D structures and motions following their initiation that accompany the local mean flow rather than the GW phase. An assessment of the momentum

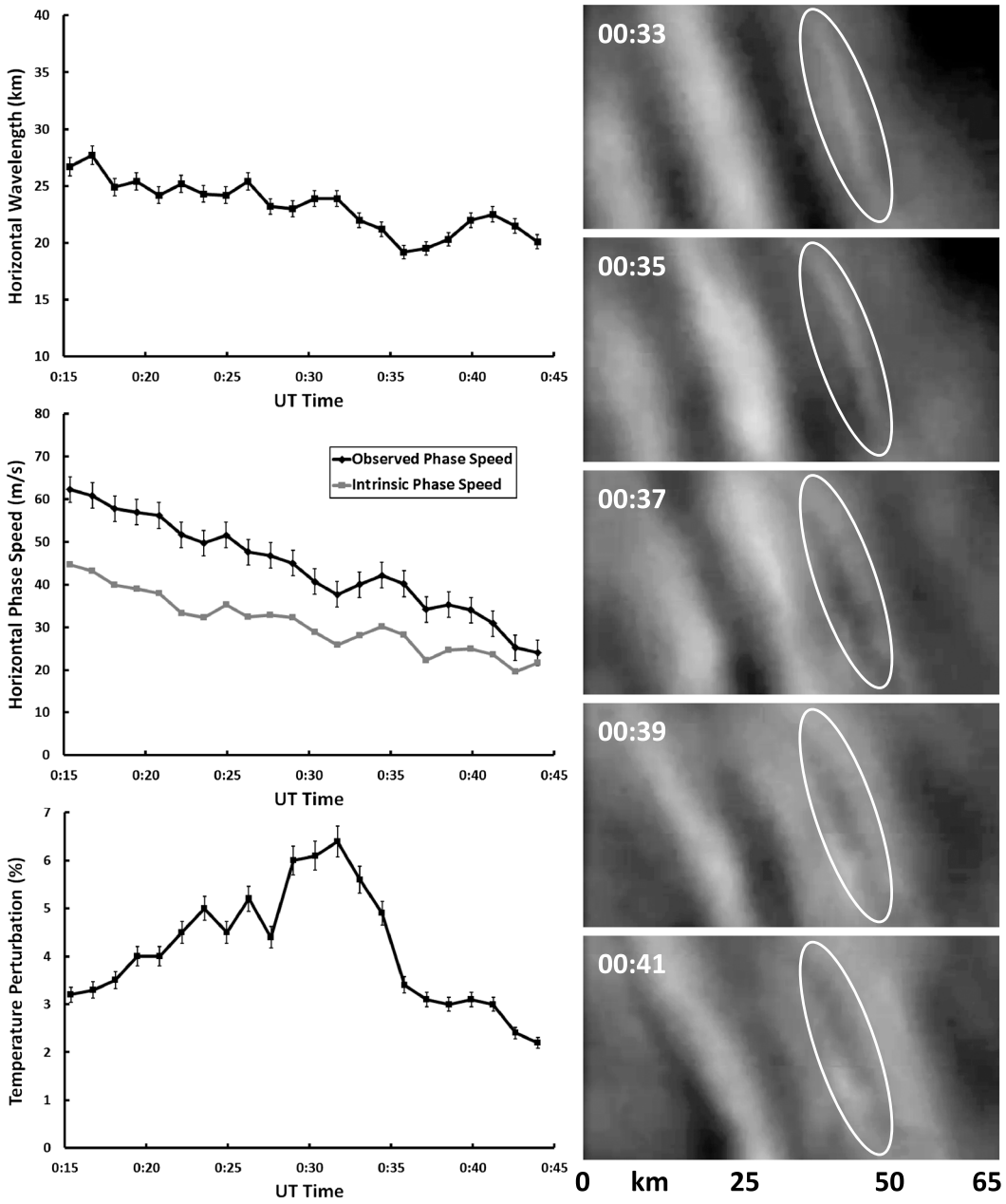

Figure 6. (left column) AMTM estimates for the Event 2 GW λ_h, c, c_i, and $< T'/T >$ at ~1.3 min intervals spanning this event. (right column) AMTM intensity images showing the initiation and evolution of an apparent instability feature accompanying the maximum GW amplitude in Event 2. Note the very different horizontal phase speed and evolution to 3-D structure accompanying this event. Error bars on the line plots in the left column show the uncertainties for 30 s estimates. Error bars are not shown for c_i because measured U uncertainties are not known. Variations at longer time scales represent geophysical variability. Spatial scales of the images are shown at the bottom right.

flux accompanying this GW is provided below. The relation of these results to previous observations and modeling of GW instability dynamics is discussed further in section 4.

We now employ the measured and inferred ~10 min GW parameters to estimate its momentum flux and tendency for instability. GW parameters obtained from the AMTM averaged from 00:25-00:31 UT are λ_h ~24 km, c ~45 m s^{-1}, c_i ~33 m s^{-1}, and $< T'>/T_0 = 0.055$. The estimate for $<T'>$ is confirmed with a fit to the measured values along the GW propagation at 00:31 UT with λ_h = 24 km, yeilding a peak $<T'>$ ~11K (see Figure 6, lower right). Together with a local mean T ~200 K, and an inferred mean and ~12h GW dT'/dz ~ −5K km^{-1}

giving N ~0.0146 s^{-1}, these yield estimates of $\omega_i = k_h c_i$ ~0.00864 s^{-1}, ω_i/N ~0.592 (confirming the estimate of ω_i/N ~0.6 from c_{ghi}/c_i above), $(1 - \omega_i^2/N^2) = 0.65$, $\lambda_z \sim \lambda_h/1.36$ ~17.6 km, C^2 ~0.324, T'/T ~0.097, u_h' ~51 m s^{-1}, w' ~37 m s^{-1}, and $< u_h'w' >$ ~940 m^2 s^{-2}. Either the dT'/dz estimate for this GW relative to the large-scale dT'/dz or the ratio u_h'/c_i ~1.5 implies $N^2 < 0$ locally within the GW field and a strongly unstable GW amplitude, hence an explanation for the observed instability structure occurring at the time of maximum amplitude. As in Event 1, additional uncertainty in these estimates accompany the uncertainty in z_{FWHM}; a 10% increase in z_{FWHM} in this case yields a ~27% increase in $< u_h'w' >$. For the parameters here, differences in H and H_p are ~6%, implying that the approximation in equation (17) is valid. Hence, the overall uncertainty in the Event 2 $< u_h'w' >$ may be ~40%, unless z_{FWHM} is larger than measured by SABER during Event 1.

Finally, performing a least squares fit of the $T'(x',y')$ field described by equation (28) to the AMTM image at 00:31 UT in Figure 4, we obtain FWHM packet dimensions of X' ~50 km and Y' ~37 km. This GW and its associated momentum flux are thus much more localized than the GW packet in Event 1 and should be expected to yield significant secondary GW generation. The relation of these estimates to previous studies and their implications for MLT dynamics will be discussed in greater detail below.

4. Discussion

Our intent in this paper is to develop and demonstrate a new quantitative method for assessing the momentum fluxes accompanying individual, small-scale GW packets identified in AMTM measurements. Previous assessments employing multiple types of data from the lower stratosphere into the MLT have suggested that the majority of GW momentum fluxes accompany GWs occurring on small spatial and temporal scales, with typically ~70% of the total momentum flux due to GWs having λ_h <100 km and intrinsic GW periods T_{GW} <1 h [e.g., *Fritts and Vincent*, 1987; *Reid and Vincent*, 1987; *Nastrom and Fritts*, 1992; *Pfister et al*., 1993]. Large-amplitude GW packets likely to contribute large momentum fluxes are also often highly localized in space and time [*Fritts and Yuan*, 1989; *Fritts et al*., 1992, 2002; *Swenson and Mende*, 1994; *Yue et al*., 2009], making them strong sources of secondary GWs penetrating to much higher altitudes [*Vadas and Fritts*, 2001, 2004]. These findings suggest that a method for quantifying the momentum fluxes and spatial localization of GW packets that can be resolved in AMTM FOVs may be able to make important contributions in quantifying both GW forcing of the MLT and the characterization of secondary GW generation accompanying these events.

4.1. Uncertainties in Airglow Estimates of GW Amplitudes

As noted earlier, the Krassovsky ratio, $\eta = (I'/I)/(T'/T)$, and the cancelation factor, CF, employed by various authors (which is similar to η, but also includes the effects of GW phase averaging across the finite OH airglow layer depth), tend to be highly variable, with dependence on temperature, pressure, species chemistry, and the GW λ_h, λ_z, and c_i [e.g., *Krassovsky*, 1972; *Viereck and Deehr*, 1989; *Hecht and Walterscheid*, 1991; *Takahashi et al*., 1992; *Hickey et al*., 1993; *Reisin and Scheer*, 1996; *Hickey and Yu*, 2005; *Taori and Taylor*, 2006; *Vargas et al*., 2007]. The observed and predicted variations are easily as large as ~2–5 or more for the GW parameters considered by various researchers [e.g., *Hickey and Yu*, 2005; *Taori and Taylor*, 2006, and references therein]. The uncertainties in η or CF also imply quadratically larger uncertainties in GW momentum flux estimates associated with the cancelation factor, CF, thus very large uncertainties for any estimation of GW momentum fluxes that relies on I'/I measurements. Indeed, *Hickey and Yu* [2005] note that CFs "… differ by factors of ~10 between models, implying factors of ~100 between derived gravity wave fluxes …" for "… phase speeds less than about 40 m s^{-1}…", and by "… factors of 2–3 …" (hence factors of up to ~10 for GW momentum fluxes) between models for phase speeds >60 m s^{-1}. Hence, estimates of GW momentum fluxes relying on OH layer I'/I measurements must be regarded as highly uncertain at present (despite the small uncertainties claimed by some authors) until further modeling and/or detailed comparisons of coincident I'/I and T'/T measurements are performed for a range of GW and environmental parameters. These results impact momentum flux estimates reported in a number of previous studies [e.g., *Swenson and Gardner*, 1998; *Swenson and Liu*, 1998; *Fritts et al*., 2002; *Liu and Swenson*, 2003; *Suzuki et al*., 2007; *Vargas et al*., 2009].

Similar issues apply to the formulation by *Gardner et al*. [1999] that has been employed by various authors [e.g., *Tang et al*., 2002, 2005a, 2005b; *Espy et al*., 2004a, 2004b, 2006]. As in *Swenson and Liu* [1998], *Gardner et al*. [1999] relate T'/T to I'/I with assumptions about the GW λ_z, its growth with altitude (which in general is highly uncertain and variable due to potential GW transience and dissipation), and the width and airglow

emission intensity of the OH layer. This dependence necessarily exhibits the same uncertainties accompanying the inference of T'/T from I'/I. However, *Gardner et al.* [1999] also employ a spectral rather than a discrete formulation that assumes a specific GW spectral form and separability of the spectral dependence on the GW azimuth of propagation, ϕ, and intrinsic frequency, ω_i. This assumption fails in cases, such as observed here, where the GW field is composed of discrete events propagating in different directions. In summary, a spectral assessment cannot describe the variances and covariances of discrete GWs.

In contrast, our expression for momentum flux based on airglow temperature perturbations in equation (21) is the same as employed by a number of previous authors [e.g., *Swenson and Gardner*, 1998; *Swenson and Liu*, 1998; *Fritts et al.*, 2002; *Liu and Swenson*, 2003; *Suzuki et al.*, 2007], except that we employ direct T'/T measurements. The advantage of equation (21) in cases where an AMTM or lidar provides a direct measure of the GW T'/T, rather than an indirect estimate from airglow I'/I variations, is that direct T'/T measurements avoid the very large uncertainties due to the uncertain relationship between T'/T and I'/I discussed by *Hickey and Yu* [2005]. These are by far the largest uncertainties in the estimates of GW momentum fluxes, as the other variables in equation (21), e.g., ω_i and N, can be determined with high confidence with combined AMTM measurements of the GW λ_h, c, and ϕ, correlative lidar measurements of $T(z)$ and inferred $N(z)$, and lidar or radar measurements of the mean wind in the plane of GW propagation, $U_h(z)$. As noted above, the AMTM defines the GW λ_h, c, ϕ, and $< T' >/T$, to within a few % for temporal averages of a few minutes. Indeed, larger uncertainties are contributed by geophysical variability over the lifetime of the events described here. Similar uncertainties pertain to the lidar and radar estimates of $T(z)$, $N(z)$, and $U_h(z)$. When averaged over the GW event duration, we estimate the cumulative uncertainty in $<u'w'>$ to be ~40% or less unless $z_{FWHM} > 7$ km, in which case $<u_h'w'>$ may be significantly larger than estimated (e.g., the uncertainties shown in Figures 3 and 5 for ~30 s estimates for Events 1 and 2 yield much smaller uncertainties spanning the GW packet durations).

4.2. Event 1 GW Evolution

The Event 1 GW observed over Logan on 6 June 2013 was an unusual GW in several respects. It appeared to arise "in situ," apparently propagating from below rather than propagating into the AMTM FOV from the SW. It exhibited a large initial amplitude and expanded horizontally to span several phase fronts from ~07 to 08 UT. This GW had a very small c over the interval shown, despite having a large c_i at these times. The large amplitude in the T' field and the large ω_i ~0.87 N imply GW velocities of u' ~8.5 m s^{-1} and w' ~14.7 m s^{-1} and a significant momentum flux, $<u_h'w'>$ ~62 m^2 s^{-2}. This GW also had an I'/I ~0.22 (implying η ~6), which is significantly larger than observed for typical GWs but significantly smaller than the event discussed by *Yamada et al.* [2001] for which the momentum flux was estimated by *Fritts et al.* [2002]. Hence, it is not surprising that the inferred momentum flux is ~5–10 times mean summer and winter solstice values at ~87 km measured by radars or inferred from middle atmosphere GCMs [e.g., *Tsuda et al.*, 1990; *Fritts and Alexander*, 2003].

Finally, the large amplitude, large ω_i, and compact spatial distribution of this GW packet of FWHM X' ~50 km have other possible implications. While the GW had $u' << c_i$, suggesting that it was not overturning, it was in the range of ω_i/N for which modulational instability is expected [*Sutherland*, 2001; *Dosser and Sutherland*, 2011], though this does not imply instability and dissipation. The strong GW packet localization also suggests significant potential excitation of secondary GWs having dominant λ_h ~100–200 km that might readily propagate to much higher altitudes [e.g., *Vadas and Fritts*, 2001, 2004; *Vadas*, 2007]. Indeed, the larger momentum fluxes accompanying less frequent, but larger-amplitude, smaller-scale GW packets may well dominate both the mean forcing of the MLT and the generation of secondary GWs having influences extending well into the thermosphere.

4.3. Event 2 GW Evolution

The small-scale Event 2 GW discussed above occurred in the presence of several larger-scale GWs, all of which appeared to contribute to the local environment influencing the propagation and character of this GW. Indeed, the ~1 h and ~4 h GWs identified here also contributed momentum fluxes comparable to or larger than mean values. Compared to the Event 1 GW, the small-scale Event 2 GW was much more transient, appeared to be strongly modulated by the ~1 h GW, and achieved a substantially larger peak momentum flux, $<u_h'w'>$ ~940 m^2 s^{-2} (~100–200 times mean values), and a larger I'/I ~0.35 (implying η ~5.5), accompanying the maximum T' of the ~1 h GW. The occurrence of transient, high-frequency GWs at the

maximum T' phase of larger-scale GWs may provide useful insights into the influences of larger-scale GWs on small-scale GW momentum transport. As noted in section 3.2, this correlation suggests the presence of a GW-induced wind shear, $du_h'/dz > 0$ at the airglow layer, with $u_h' > 0$ in the direction of propagation of the larger-scale GW that will influence the ω_i and potentially the vertical propagation of the smaller-scale GW.

The very large inferred peak momentum flux for the Event 2 GW is significantly larger than all previous estimates except that by *Fritts et al*. [2002] for the GW breaking event described by *Yamada et al*. [2001], which had I'/I ~0.55 and a somewhat smaller inferred momentum flux of $< u_h'w' >$ ~900 m^2 s^{-2}. Indeed, these two events exhibit a number of similarities. These include the following: (1) very similar inferred GW velocities: u_h' ~51 m s^{-1}, w' ~37 m s^{-1}, and u_h'/c_i ~1.5 for Event 2; u_h' ~50 m s^{-1}, w' ~36 m s^{-1}, and u_h'/c_i ~1 for the *Yamada et al*. [2001] event; (2) very similar spatial scales and ω_i/N: λ_h ~24 km, X' ~50 km, and ω_i/N ~0.592 for Event 2; λ_h ~27 km, X' ~60 km, and ω_i/N ~0.5 for the *Yamada et al*. [2001] event; and (3) rapid GW breakdown following initial instability: likely within ~2 buoyancy periods, T_b, though initial instability is not captured in the *Yamada et al*. [2001] image sequence and the latter stages of instability are not seen in Event 2.

4.4. Implications of Large-Amplitude Events

The similarities of the two events described here, and the GW breaking event examined by *Yamada et al*. [2001] and *Fritts et al*. [2002], particularly their small spatial and temporal scales, suggest that such events may be important but challenging to identify and quantify in a routine fashion. If such events are more common and simply not recognized, however, they may well play major roles in momentum transport and deposition in the MLT and in the radiation of secondary GWs to higher altitudes that are not fully appreciated at present. Additional evidence for large-amplitude dynamics is available from various radars and lidars that have provided previous velocity and temperature measurements in the MLT. As examples, *Fritts and Vincent* [1987] reported GW momentum flux modulations by the diurnal tide observed over Adelaide, Australia, with an MF radar having magnitudes as large as ±30 m^2 s^{-2}; *Reid et al*. [1988] reported a 3 h averaged momentum flux magnitude of ~66 m^2 s^{-2} observed with the sounding system (radar) VHF radar at Andenes, Norway; and *Fritts et al*. [1992] described measurements at the Jicamarca Radio Observatory exhibiting >15 m s^{-1} velocity perturbations at a zenith angle of 2.5° and an ~60 m^2 s^{-2} momentum flux for a 1 h interval. Very large w' and T', ~30 m s^{-1} and ~20 K, respectively, for a high-frequency GW (observed period ~8 min) have also been observed previously with the ALOMAR sodium lidar (B. Williams, personal communication, 2014).

Summarizing, strong and very strong events contributing significantly to total GW momentum transport and deposition are likely not rare, and imager and AMTM measurements spanning a larger part of the MLT than can be accomplished with radars or lidars provide a viable means of describing their statistics. A broader survey and quantification of strong events would help determine the statistics, scales, and consequences of their influences at MLT altitudes.

5. Summary and Conclusions

We have developed a procedure for quantifying the momentum fluxes associated with localized GW packets having small horizontal wavelengths and potentially small packet widths that are challenging or impossible to quantify with traditional radars, lidars, and/or airglow imagers. This procedure employs the new AMTMs and correlative sodium lidar and/or radar measurements to quantify both the GW environment and all of the intrinsic properties for GW packets that may or may not be contained entirely within an AMTM FOV. Specifically, AMTMs provide accurate estimates of GW λ_h, c, ϕ, and $< T'/T >$ on short time scales. Sodium lidars provide radial winds, $u_r(z)$, and $T(z)$ in several beams, hence $U_h(z)$, $T_0(z)$, $T'(z)$, GW c_i (together with AMTM c), and estimates of u', v', and/or w'. Finally, VHF, MF, or meteor radars provide large-scale winds, yielding $U_h(z)$, large-scale GW $u'(z)$ and $v'(z)$, and potentially the small-scale GW $u_r'(z)$ in the case of narrow-beam radars.

We have applied our momentum flux estimation procedure to two small-scale GW events observed in June 2013 over Logan, Utah and in January 2014 over ALOMAR in northern Norway. Each GW event was characterized by a small λ_h, a small packet width, X', in the plane of GW propagation, a large AMTM amplitude, $<T'/T>$, a high intrinsic frequency, ω_i/N ~0.6–0.87, and a large or very large inferred momentum flux, $< u_h'w' >$ ~62 and 940 m^2 s^{-2}, respectively. These estimates are substantially larger than the mean GW momentum fluxes expected at MLT altitudes under solstice conditions provided by previous measurements (primarily radars) and inferred from large-scale models.

Identical capabilities exist with similar combinations of an airglow imager, sodium (or other resonance) lidar, and MLT radar, *except for quantification of the GW* $< T'/T >$. But this is by far the most critical measurement in quantifying momentum fluxes and cannot currently be estimated with the needed precision by airglow imagers providing only I'/I. Lidars and radars likewise can provide momentum flux estimates using the dual-beam method of *Vincent and Reid* [1983] or its extension to multiple beams. But such measurements depend on certain assumptions, especially the requirement for statistical homogeneity of the GW field in all lidar or radar beams. However, this is *almost certainly not satisfied* for small-scale GW packets by lidars and radars having off-zenith beam angles of 15–20°, for which beam separations at ~90 km are 45–60 km and likely not small compared to GW packet dimensions. To the extent that small-scale GW packets contribute significantly to the MLT momentum budget, neither airglow imagers, lidars, nor radars can be expected to characterize the statistics of such small-scale GW events or their implications for secondary GW generation influencing higher altitudes. Spatial and/or temporal localization of small-scale, large-amplitude GWs could also have contributed errantly to some of the large momentum flux estimates by radars cited above, if GW packet localization caused the assumption of statistical homogeneity at different beams to be violated.

Our measurements of GW packet characteristics and momentum fluxes discussed in this paper raise the question of what fraction of the total momentum flux might accompany such large-amplitude, small-scale GWs, and what are the implications for MLT structure, variability, secondary GW generation, and parameterization of the influences of these dynamics. The implications of a large fraction of the total momentum flux due to such GWs would be significant, yet we have a poor understanding of the statistics of such events at present. The occurrence of small numbers of very strong events is similar to inferences of infrequent, strong mountain wave responses from constant-pressure balloons in the stratosphere by *Hertzog et al.* [2012]. In the MLT, however, propagation conditions appear to also play a major, and perhaps dominant, role. Hence, we believe an assessment of the statistics of such events should be considered a high priority for correlative MLT measurements able to perform such studies.

Finally, AMTMs offer the potential to measure the spatial and temporal distributions of momentum flux for GW packets confined within the FOV. Quantification of the GW parameters also yields an estimate of the vertical group velocity, c_{gz}, given in equation (29), hence also the vertical extent of the GW packet, from its observed duration. This enables an estimate of the total momentum accompanying the GW packet arising from its transient momentum flux divergence, or more generally, the Eliassen-Palm (EP) flux divergence [*Warner and McIntyre*, 1999], at each location. Such measurements would also enable direct estimates of the spatial scales of body forces yielding generation of secondary GWs that have the potential to propagate to much higher altitudes.

Acknowledgments

Support for this research was provided by NSF grants AGS-1136269, AGS-1259136, AGS-1042227, and AGS-1135882. The AMTM was designed at USU and the USURF Space Dynamics Laboratory under an Air Force DURIP grant F-49620-02-1-0258. We are most grateful to W.R. Pendleton, Jr., R. Esplin, and D. Mclain for their considerable help with the AMTM development and testing. We thank three anonymous reviewers for very helpful comments on the manuscript. Finally, we acknowledge facility support by the Institute of Atmospheric Physics in Germany, and the ALOMAR Observatory in Norway. AMTM and lidar data are extensive. Hence, only 1 h lidar wind and temperature profiles and AMTM keograms are provided to the NSF CEDAR MADRIGAL database. Researchers wishing to explore collaborative activities with additional data are encouraged to contact Dave Fritts at dave@gats-inc.com or Mike Taylor at Mike.Taylor@usu.edu.

References

Baker, D. J., and A. T. Stair (1988), Rocket measurements of the altitude distribution of the hydroxyl airglow, *Phys. Scr.*, *37*, 611–622.

Baumgaertner, A. J. G., M. J. Jarvis, A. J. McDonald, and G. J. Fraser (2006), Observations of the wavenumber 1 and 2 components of the semi-diurnal tide over Antarctica, *J. Atmos. Sol. Terr. Phys.*, *68*, 1195–1214.

Booker, J. R., and F. P. Bretherton (1967), The critical layer for internal gravity waves in a shear flow, *J. Fluid Mech.*, *27*(3), 13–539.

Dosser, H. V., and B. R. Sutherland (2011), Weakly nonlinear bob-Boussinesq internal gravity wavepackets, *Phys. D*, *240*, 346–356, doi:10.1016/j.physd.2010.09.008.

Ejiri, M. K., K. Shiokawa, T. Ogawa, K. Igarashi, T. Nakamura, and T. Tsuda (2003), Statistical study of short-period gravity waves in OH and OI nightglow images at two separated sites, *J. Geophys. Res.*, *108*(D21), 4679, doi:10.1029/2002JD002795.

Espy, P. J., G. O. L. Jones, G. R. Swenson, J. Tang, and M. J. Taylor (2004a), Tidal modulation of the gravity-wave momentum flux in the Antarctic mesosphere, *Geophys. Res. Lett.*, *31*, L11111, doi:10.1029/2004GL019624.

Espy, P. J., G. O. L. Jones, G. R. Swenson, J. Tang, and M. J. Taylor (2004b), Seasonal variations of the gravity wave momentum flux in the Antarctic mesosphere and lower thermosphere, *J. Geophys. Res.*, *109*, D23109, doi:10.1029/2003JD004446.

Espy, P. J., R. E. Hibbins, G. R. Swenson, J. Tang, M. J. Taylor, D. M. Riggin, and D. C. Fritts (2006), Regional variations of mesospheric gravity wave momentum fluxes over Antarctica, *Ann. Geophys.*, *24*, 81–88, SRef-ID: 1432-0576/ag/2006-24-81.

Fritts, D. C. (1984), Gravity wave saturation in the middle atmosphere: A review of theory and observations, *Rev. Geophys. Space Phys.*, *22*, 275–308.

Fritts, D. C., and M. J. Alexander (2003), Gravity dynamics and effects in the middle atmosphere, *Rev. Geophys.*, *41*(1), 1003, doi:10.1029/2001RG000106.

Fritts, D. C., and T. Lund (2011), Gravity wave influences in the thermosphere and ionosphere: Observations and recent modeling, in *Aeronomy of the Earth's Atmosphere and Ionosphere*, edited by M. Abdu and D. Pancheva, pp. 109–130, Springer, Sopron, Hungary.

Fritts, D. C., and R. A. Vincent (1987), Mesospheric momentum flux studies at Adelaide, Australia: Observations and a gravity wave/tidal interaction model, *J. Atmos. Sci.*, *44*, 605–619.

Fritts, D. C., and L. Yuan (1989), Measurement of momentum fluxes near the summer mesopause at Poker Flat, Alaska, *J. Atmos. Sci.*, *46*, 2569–2579.

Fritts, D. C., L. Yuan, M. H. Hitchman, L. Coy, E. Kudeki, and R. F. Woodman (1992), Dynamics of the equatorial mesosphere observed using the Jicamarca MST radar during June and August 1987, *J. Atmos. Sci.*, *49*, 2353–2371.
Fritts, D. C., S. A. Vadas, and Y. Yamada (2002), An estimate of strong local gravity wave body forcing based on OH airglow and meteor radar observations, *Geophys. Res. Lett.*, *29*(10), 1429, doi:10.1029/2001GL013753.
Fritts, D. C., D. Janches, H. Iimura, W. K. Hocking, N. J. Mitchell, B. Fuller, B. Vandepeer, J. Hormaechea, C. Brunini, and H. Levato (2010), Southern Argentina agile meteor radar (SAAMER): System design and initial measurements of large-scale winds and tides, *J. Geophys. Res.*, *115*, D18112, doi:10.1029/2010JD013850.
Gardner, C. S., K. Gulati, Y. Zhao, and G. R. Swenson (1999), Measuring gravity wave momentum fluxes with airglow images, *J. Geophys. Res.*, *104*, 11,903–11,915, doi:10.1029/1999JD900105.
Hecht, J. H., and R. L. Walterscheid (1991), Observation of the OH Meinel (6,2) and O_2 atmospheric (0,1) nightglow emission from Maui during the ALOHA-90 campaign, *Geophys. Res. Lett.*, *18*, 1341–1344, doi:10.1029/91GL01152.
Hecht, J. H., R. L. Walterscheid, D. C. Fritts, J. R. Isler, D. C. Senft, C. S. Gardner, and S. J. Franke (1997), Wave breaking signatures in OH airglow and sodium densities and temperatures. Part I: Airglow imaging, Na lidar, and MF radar observations, *J. Geophys. Res.*, *102*, 6655–6668, doi:10.1029/96JD02619.
Hecht, J. H., C. Fricke-Bergemann, and R. L. Walterscheid (2000), Observations of the breakdown of an atmospheric gravity wave near the cold summer mesopause at 54N, *Geophys. Res. Lett.*, *27*, 879–882, doi:10.1029/1999GL010792.
Hertzog, A., G. Boccara, R. A. Vincent, F. Vial, and P. Cocquerez (2008), Estimation of gravity wave momentum flux and phase speeds from quasi-Lagrangian stratospheric balloons flights. Part 2: Results from the Vorcore campaign in Antarctica, *J. Atmos. Sci.*, *65*, 3056–3070, doi:10.1175/2008JAS2710.1.
Hertzog, A., M. J. Alexander, and R. Plougonven (2012), On the intermittency of gravity wave momentum flux in the stratosphere, *J. Atmos. Sci.*, *69*, 3433–3448, doi:10.1175/JAS-D-12-09.1.
Hickey, M. P., and Y. Yu (2005), A full-wave investigation of the use of a "cancellation factor" in gravity wave-OH airglow interaction studies, *J. Geophys. Res.*, *110*, A01301, doi:10.1029/2003JA010372.
Hickey, M. P., G. Schubert, and R. L. Walterscheid (1993), Gravity wave driven fluctuations in the O_2 atmospheric (0–1) nightglow from an extended, dissipative emission region, *J. Geophys. Res.*, *98*, 13,717–13,729, doi:10.1029/92JA02348.
Horinouchi, T., T. Nakamura, and J. Kosaka (2002), Convectively generated mesoscale gravity waves simulated throughout the middle atmosphere, *Geophys. Res. Lett.*, *29*(21), 2007, doi:10.1029/2002GL016069.
Kim, Y.-J., S. D. Eckermann, and H.-Y. Chun (2003), An overview of the past, present, and future of gravity-wave drag parameterization for numerical climate and weather prediction models, *Atmos. Ocean*, *41*(1), 65–98.
Krassovsky, V. I. (1972), Infrasonic variations of OH emission in the upper atmosphere, *Ann. Geophys.*, *28*, 739–746.
Lane, T. P., M. J. Reeder, and T. L. Clark (2001), Numerical modeling of gravity wave generation by deep tropical convection, *J. Atmos. Sci.*, *58*(10), 1249–1274.
Li, F., A. Z. Liu, G. R. Swenson, J. H. Hecht, and W. A. Robinson (2005), Observations of gravity wave breakdown into ripples associated with dynamical instabilities, *J. Geophys. Res.*, *110*, D09S11, doi:10.1029/2004JD004849.
Li, T., C. Y. She, H.-L. Liu, and M. Montgomery (2007), Evidence of a gravity wave breaking event and the estimation of the wave characteristics from sodium lidar observation over Fort Collins, CO (41°N, 105°W), *Geophys. Res. Lett.*, *34*, L05815, doi:10.1029/2006GL028988.
Lilly, D. K., and P. J. Kennedy (1973), Observations of a stationary mountain wave and its associated momentum flux and energy dissipation, *J. Atmos. Sci.*, *30*, 1135–1152.
Liu, A. Z., and G. R. Swenson (2003), A modeling study of O_2 and OH airglow perturbations induced by atmospheric gravity waves, *J. Geophys. Res.*, *108*(D4), 4151, doi:10.1029/2002JD002474.
Lund, T., and D. C. Fritts (2012), Gravity wave breaking and turbulence generation in the thermosphere, *J. Geophys. Res.*, *117*, D21105, doi:10.1029/JD017536.
McIntyre, M. E. (1981), On the 'wave momentum' myth, *J. Fluid Mech.*, *106*, 331–347.
Murphy, D. J., et al. (2006), A climatology of tides in the Antacrtic mesosphere, *J. Geophys. Res.*, *111*, D23104, doi:10.1029/2005JD006803.
Nakamura, T., A. Higashikawa, T. Tsuda, and Y. Matsushita (1999), Seasonal variations of gravity wave structures in OH airglow with a CCD imager at Shigaraki, *Earth Planets Space*, *51*, 897–906.
Nakamura, T., T. Aono, T. Tsuda, A. G. Admiranto, E. Achmad, and Suratno (2003), Mesospheric gravity waves over a tropical convective region observed by OH airglow imaging in Indonesia, *Geophys. Res. Lett.*, *30*(17), 1882, doi:10.1029/2003GL017619.
Nappo, C. J. (2002), *Atmospheric Gravity Waves*, *Int. Geophys. Ser.*, vol. 85, Academic Press, Amsterdam.
Nastrom, G. D., and D. C. Fritts (1992), Sources of mesoscale variability of gravity waves. I: Topographic excitation, *J. Atmos. Sci.*, *49*, 101–110.
Pautet, P.-D., M. J. Taylor, Y. Zhao, T. Yuan, W. R. Pendleton Jr., R. Esplin, and D. McLain (2014), An advanced mesospheric temperature mapper for high-latitude airglow studies, *Appl. Opt.*, *53*(26), 5934–5943.
Pfister, L., S. Scot, M. Loewenstein, S. Bowen, and M. Legg (1993), Mesoscale disturbances in the tropical stratosphere excited by convection: Observations and effects on the stratospheric momentum budget, *J. Atmos. Sci.*, *50*(8), 1058–75.
Plougonven, R., A. Hertzog, and H. Teitelbaum (2008), Observations of a large-amplitude mountain wave breaking over the Antarctic Peninsula, *J. Geophys. Res.*, *113*, D16113, doi:10.1029/2007JD009739.
Plougonven, R., A. Hertzog, and L. Guez (2013), Gravity waves over Antarctica and the Southern Ocean, *Q. J. R. Meteorol. Soc.*, *139*, 101–118, doi:10.1002/qj.1965.
Reid, I. M., and R. A. Vincent (1987), Measurements of mesospheric gravity wave momentum fluxes and mean flow accelerations at Adelaide, Australia, *J. Atmos. Terr. Phys.*, *49*, 443–460.
Reid, I. M., R. Rüster, P. Czechowsky, and G. Schmidt (1988), VHF radar measurements of momentum flux in the summer polar mesosphere over Andenes (69°N, 16°E), Norway, *Geophys. Res. Lett.*, *15*, 1263–1266, doi:10.1029/GL015i011p01263.
Reisin, E. R., and J. Scheer (1996), Characteristics of atmospheric waves in the tidal period range derived from zenith observations of O_2 (0–1) atmospheric and OH (6–2) airglow at lower midlatitudes, *J. Geophys. Res.*, *101*, 21,223–21,232, doi:10.1029/96JD01723.
Simkhada, D. B., J. B. Snively, M. J. Taylor, and S. J. Franke (2009), Analysis and modeling of ducted and evanescent gravity waves observed in the Hawaiian airglow, *Ann. Geophys.*, *27*, 3213–3224, ISEA special issue, April, 2009.
Smith, R. B., B. K. Woods, J. Jensen, W. A. Cooper, J. D. Doyle, Q. Jiang, and V. Grubisic (2008), Mountain waves entering the stratosphere, *J. Atmos. Sci.*, *65*, 2543–2562.
Smith, S., J. Baumgardner, and M. Mendillo (2009), Evidence of mesospheric gravity-waves generated by orographic forcing in the troposphere, *Geophys. Res. Lett.*, *36*, L08807, doi:10.1029/2008GL036936.
Sutherland, B. R. (2001), Finite-amplitude internal wavepacket dispersion and breaking, *J. Fluid Mech.*, *429*, 343–380.

Sutherland, B. R. (2006), Internal wave instability: Wave-wave versus wave-induced mean flow interactions, *Phys. Fluids*, *18*, 074107, doi:10.1063/1.2219102.
Suzuki, S., K. Shiokawa, Y. Otsuka, T. Ogawa, and P. Wilkinson (2004), Statistical characteristics of gravity waves observed by an all-sky imager at Darwin, Australia, *J. Geophys. Res.*, *109*, D20S07, doi:10.1029/2003JD004336.
Suzuki, S., K. Shiokawa, Y. Otsuka, T. Ogawa, M. Kubota, M. Tsutsumi, T. Nakamura, and D. C. Fritts (2007), Gravity wave momentum flux in the upper mesosphere derived from OH airglow imaging measurements, *Earth Planets Space*, *59*, 421–428.
Swenson, G. R., and C. S. Gardner (1998), Analytical models for the responses of the mesospheric OH* and Na layers to atmospheric gravity waves, *Geophys. Res. Lett.*, *25*, 477–480, doi:10.1029/98GL00132.
Swenson, G. R., and A. Z. Liu (1998), A model for calculating acoustic gravity wave energy and momentum flux in the mesosphere from OH airglow, *Geophys. Res. Lett.*, *25*(4), 477–480, doi:10.1029/98GL00132.
Swenson, G. R., and S. B. Mende (1994), OH emission and gravity waves (including a breaking wave) in all-sky imagery from Bear Lake, UT, *Geophys. Res. Lett.*, *21*, 2239–2242, doi:10.1029/94GL02112.
Swenson, G. R., R. Haque, W. Yang, and C. S. Gardner (1999), Momentum and energy fluxes of monochromatic gravity waves observed by an OH imager at Starfire Optical Range, New Mexico, *J. Geophys. Res.*, *104*(D6), 6067–6080, doi:10.1029/1998JD200080.
Takahashi, H., Y. Sahai, P. P. Batista, and B. R. Clemesha (1992), Atmospheric gravity wave effect on the airglow O_2 (0–1) and OH (9–4) band intensity and temperature variations observed from a low latitude station, *Adv. Space Res.*, *12*, (10)131–(10)134.
Tang, J., A. Z. Liu, and G. R. Swenson (2002), High frequency gravity waves observed in OH airglow at Starfire Optical Range, NM: Seasonal variations in momentum flux, *Geophys. Res. Lett.*, *29*(20), 1996, doi:10.1029/2002GL015794.
Tang, J., F. Kamalabadi, S. J. Franke, A. Z. Liu, and G. R. Swenson (2005a), Estimation of gravity wave momentum flux with spectroscopic imaging, *IEEE Trans. Geosci. Remote Sens.*, *43*, 103–109.
Tang, J., G. R. Swenson, A. Z. Liu, and F. Kamalabadi (2005b), Observational investigations of gravity wave momentum flux with spectroscopic imaging, *J. Geophys. Res.*, *110*, D09S09, doi:10.1029/2004JD004778.
Taori, A., and M. J. Taylor (2006), Characteristics of wave induced oscillations in mesospheric O_2 emission intensity and temperatures, *Geophys. Res. Lett.*, *33*, L01813, doi:10.1029/2005GL024442.
Taylor, M. J., and M. A. Hapgood (1988), Identification of a thunderstorm as a source of short period gravity waves in the upper atmospheric airglow emissions, *Planet. Space Sci.*, *36*(10), 975–985.
Taylor, M. J., M. B. Bishop, and V. Taylor (1995), All-sky measurements of short-period waves imaged in the OI(557.7 nm), Na(589.2 nm), and near-infrared OH and O_2(0, 1) nightglow emissions during the ALOHA-93 campaign, *Geophys. Res. Lett.*, *22*, 2833–2836, doi:10.1029/95GL02946.
Taylor, M. J., W. R. Pendleton Jr., S. Clark, H. Takahashi, D. Gobbi, and R. A. Goldberg (1997), Image measurements of short-period gravity waves at equatorial latitudes, *J. Geophys. Res.*, *102*(D22), 26,283–26,299, doi:10.1029/96JD03515.
Tsuda, T., Y. Murayama, M. Yamamoto, S. Kato, and S. Fukao (1990), Seasonal variation of momentum flux in the mesosphere observed with the MU radar, *Geophys. Res. Lett.*, *17*, 725–728, doi:10.1029/GL017i006p00725.
Vadas, S. L. (2007), Horizontal and vertical propagation, and dissipation of gravity waves in the thermosphere from lower atmospheric and thermospheric sources, *J. Geophys. Res.*, *112*, A06305, doi:10.1029/2006JA011845.
Vadas, S. L., and D. C. Fritts (2001), Gravity wave radiation and mean responses to local body forces in the atmosphere, *J. Atmos. Sci.*, *58*, 2249–2279.
Vadas, S. L., and D. C. Fritts (2002), The importance of spatial variability in the generation of secondary gravity waves from local body forces, *Geophys. Res. Lett.*, *29*(20), 1984, doi:10.1029/2002GL015574.
Vadas, S. L., and D. C. Fritts (2004), Thermospheric responses to gravity waves arising from mesoscale convective complexes, *J. Atmos. Sol. Terr. Phys.*, *66*, 781–804.
Vargas, F., G. Swenson, A. Liu, and D. Gobbi (2007), O(1S), OH, and O_2(b) airglow layer perturbations due to AGWs, and their implied effects on the atmosphere, *J. Geophys. Res.*, *112*, D14102, doi:10.1029/2006JD007642.
Vargas, F., D. Gobbi, H. Takahashi, and L. M. Lima (2009), Gravity wave amplitudes and momentum fluxes inferred from OH airglow intensities and meteor radar winds during SpreadFEx, *Ann. Geophys.*, *27*, 2361–2369.
Viereck, R. A., and C. S. Deehr (1989), On the interaction between gravity waves and the OH Meinel (6–2) and O_2 atmospheric (0–1) bands in the polar night airglow, *J. Geophys. Res.*, *94*, 5397–5404, doi:10.1029/JA094iA05p05397.
Vincent, R. A., and I. M. Reid (1983), HF Doppler measurements of mesospheric momentum fluxes, *J. Atmos. Sci.*, *40*, 1321–1333.
Walterscheid, R. L., J. H. Hecht, R. A. Vincent, I. M. Reid, J. Woithe, and M. P. Hickey (1999), Analysis and interpretation of airglow and radar observations of quasi-monochromatic gravity waves in the upper mesosphere and lower thermosphere over Adelaide, Australia (35°S, 138°E), *J. Atmos. Terr. Phys.*, *61*, 461–478.
Warner, C. D., and M. M. E. McIntyre (1999), Toward an ultra-simple spectral gravity wave parameterization for general circulation models, *Earth Planets Space*, *51*, 475–484.
Williams, B. P., D. C. Fritts, C. Y. She, G. Baumgarten, and R. A. Goldberg (2006), Gravity wave propagation, tidal interaction, and instabilities in the mesosphere and lower thermosphere during the winter 2003 MaCWAVE rocket campaign, *Ann. Geophys.*, *24*, 1199–1208, SRef-ID: 1432-0576/ag/2006-24-1199.
Wrasse, C. M., et al. (2006), Reverse ray tracing of the mesospheric gravity waves observed at 23°S (Brazil) and 7°S (Indonesia) in airglow imagers, *J. Atmos. Terr. Phys.*, *68*, 163–181.
Xu, J., A. K. Smith, R. L. Collins, and C.-Y. She (2006), Signature of an overturning gravity wave in the mesospheric sodium layer: Comparison of a nonlinear photochemical-dynamical model and lidar observations, *J. Geophys. Res.*, *111*, D17301, doi:10.1029/2005JD006749.
Xu, X., A. H. Manson, C. E. Meek, C. Jacobi, C. M. Hall, and J. R. Drummond (2011), Mesospheric wind semidiurnal tides within the Canadian Middle Atmosphere Model Data Assimilation System, *J. Geophys. Res.*, *116*, D17102, doi:10.1029/2011JD015966.
Yamada, Y., H. Fukunishi, T. Nakamura, and T. Tsuda (2001), Breakdown of small-scale quasi-stationary gravity wave and transition to turbulence observed in OH airglow, *Geophys. Res. Lett.*, *28*, 2153–2156, doi:10.1029/2000GL011945.
Yue, J., et al. (2009), A study of OH imager observed concentric gravity waves near Fort Collins on 11 May 2004, *J. Geophys. Res.*, *114*, D06104, doi:10.1029/2008JD011244.
Zhang, X., J. M. Forbes, and M. E. Hagan (2010a), Longitudinal variation of tides in the MLT region: 1. Tides driven by tropospheric net radiative heating, *J. Geophys. Res.*, *115*, A06316, doi:10.1029/2009JA014897.
Zhang, X., J. M. Forbes, and M. E. Hagan (2010b), Longitudinal variation of tides in the MLT region: 2. Relative effects of solar radiative and latent heating, *J. Geophys. Res.*, *115*, A06317, doi:10.1029/2009JA014898.